Efficient Control of an AUV-Manipulator System: An Application for the Exploration of Europa

Brian Lynch and Alex Ellery

***Abstract*—Autonomous control of a robotic manipulator mounted on a submersible autonomous underwater vehicle (AUV) is simulated with various strategies employing combinations of feedback and feedforward control. Feedforward compensation of the manipulator motion is accomplished using a model of the system kinematics and dynamics. Hydrodynamic effects including drag, buoyancy, and added mass, as well as the reaction of the vehicle, are all compensated. Effective manipulator position control is accomplished through stabilization of the vehicle orientation and system barycenter. Stabilization of the vehicle position using feedback and/or feedforward control is also considered for comparison. Compensation of the hydrodynamic effects while stabilizing the vehicle orientation and allowing vehicle translation resulted in a significant reduction in power consumption. Although experimental verification of the results is required, the improvement in efficiency may be beneficial for submersible vehicles operating in extremely remote conditions or extraterrestrial environments such as the oceans of Jupiter's moon, Europa.**

***Index Terms*—Autonomous underwater vehicle (AUV), Europa, feedforward control, remotely operated vehicle (ROV), robotic manipulator, stabilization.**

I. Introduction

EXPLORATION of the icy moons of the gas giants—specifically Europa and Enceladus—has become attractive by virtue of their astrobiological potential, despite the huge engineering challenges. Although the future of the proposed European Laplace mission is uncertain, the scientific case for exploring Europa remains a high priority. So it is Europa, one of the Galilean moons of Jupiter, that we will adopt as our primary target, though much of the material presented here will be applicable to Enceladus (though Enceladus is not expected to possess hydrothermal vents). There are, in addition, potential terrestrial testing environments that are partially analogous to Europa (Antarctic subglacial lakes) which have high scientific value in themselves, e.g., Lake Vostok [1] and Lake Ellsworth [2]. Europa, like its companion moons Io and Ganymede, lies locked in gravitational resonance with Jupiter. The eccentric orbit generates tidal stresses in the mantle of ice which melts to form a subsurface ocean of liquid water. Europa and its companions Ganymede and Callisto are believed to possess subsurface liquid water oceans beneath their icy crusts [3]. The low cratering density of the surface of Europa suggests that its surface is young (less than 50 million years) indicating extensive resurfacing from below. While the Ganymede ocean is believed to be locked below 150 km of overlying ice, Europa's subsurface ocean may be as close as 1–10 km from the surface. Penetrating this crust is not addressed here but a number of approaches have been proposed [4]–[6]. Europa's water ocean is believed to span over 100 km in depth, reaching to its silicate core. If so, it is plausible that hydrothermal vents may exist at the interface between the silicate core and liquid water mantle similar to those at the ocean depths on Earth. The pressure at the base of this ocean would be approximately 85–200 MPa depending on the ice shell thickness.

In hydrothermal vents, water circulates through buried hot volcanic fissures where it chemically reacts with the rock. Metals and sulphur precipitate out as metal sulphides forming chimneys around these vents. Ice rafts and doming of the Europan surface suggest that hydrothermal convection may be occurring and neighboring Io suggests that there may be active volcanism. At hydrothermal vents, geothermal energy is converted into chemical energy which may be exploited by chemolithotrophic bacteria as sources of free energy for the production of organic carbon [7]. These are of potential astrobiological significance [8]. Indeed, hydrothermal vents have been implicated in the origin of life on Earth [9]–[11]. Hydrothermal vent systems are the most viable candidate sites for reliable prebiotic synthesis of amino acids during the initial development of living organisms [12]. It is generally postulated that the last universal common ancestor (LUCA) of both archaea and bacteria was hydrothermophilic similar to the archaea that currently inhabit hydrothermal vents [13]. Hydrothermophilic bacteria which inhabit terrestrial hydrothermal vents are chemolithoautotrophic and use dissolved carbon dioxide as a carbon source and inorganic energy sources. Sulpholobalus shibatae can metabolize sulphide ores such as pyrite in acid environments making it a potential analog for Europan microfauna [14]. It is these hydrothermal vent locations that are of interest here; the specific problem we address is station keeping of a submersible vehicle during *in situ* investigation of hydrothermal vent chimneys using a robotic manipulator.

Oceanographic submersibles are used as the model for a Europan exploration vehicle despite the pressure at the base of the 200-km-deep ocean being approximately 3 kbar (three times greater than at the Marianas Trench). Remotely operated vehicles (ROVs) can provide mobile but stable rigs as robotic drilling platform which are remotely controlled from surface

Manuscript received October 19, 2011; revised July 17, 2012, January 14, 2013, and April 14, 2013; accepted June 19, 2013. Date of publication October 17, 2013; date of current version July 10, 2014.

Associate Editor: F. Hover.

The authors are with the Department of Mechanical & Aerospace Engineering, Carleton University, Ottawa, ON K1S 5B6 Canada (e-mail: blynch@connect.carleton.ca; aellery@mae.carleton.ca).

Digital Object Identifier 10.1109/JOE.2013.2271390

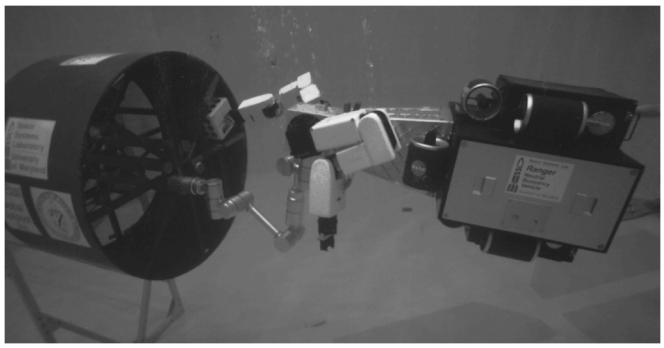

Fig. 1. Ranger neutral buoyancy vehicle (right) manipulating a satellite mockup [16].

ships. ROVs are often used as verification models for space robotic systems, e.g., the Neutral Buoyancy Vehicle (NBV) of the University of Maryland Space Systems Laboratory (College Park, MD, USA) with its dexterous manipulators [15], as shown in Fig. 1.

Autonomous underwater vehicles (AUV) dispense with the tether to the surface ship and provide greater deployment flexibility but reduced mission lifetime due to battery limitations. Primarily, AUVs have been used for sea surveys but are beginning to be deployed for more sophisticated manipulation tasks. For subsurface Europan exploration, we envisage an autonomous submersible akin to the Ranger NBV rather than the proposed miniature autonomous submersible explorer (MASE) [17]. Ranger possesses two 8-degree-of-freedom (8-DOF) arms, a 7-DOF manipulator leg, and a 6-DOF manipulator to actuate a stereocamera pair which supports a telepresence control interface (virtual reality based). However, the design and construction of such a submersible is not the concern here. We are also not concerned with the problem of vehicle trajectory generation or navigation [18], [19]. We address the problem of station keeping only while operating a single mounted manipulator investigating adjacent to the chimney of a hydrothermal vent to acquire samples for scientific analysis. This will introduce significant vehicle–manipulator coupling to the problem of position control [20], [21]. This corresponds to maneuvering as opposed to cruising in Webb's taxonomy [22]. We assume that ocean current velocity is negligible which allows the application of a spacecraft-manipulator model [23], [24]. Separation of translation and rotation is achieved by emplacement of the vehicle thrusters relative to the vehicle center of mass and center of pressure. A minimum of three pairs of thruster jets require active control to stabilize the platform while a manipulator takes samples. Thruster propulsion is based on electric motor-driven ducted propellers. A free-flyer AUV controlled in all three rotational axes using a proportional–derivative (PD) controller driving the thrusters for each axis is assumed. We assume that hydrodynamic forces and gravity/buoyancy effects can be feedforward compensated through modeling akin to the computed torque control method. It is assumed that the Europan submersible is small in size with rapid response to actuator commands for station-keeping.

The kinematics and dynamics of a robotic manipulator mounted on a submersible vehicle are coupled with the kinematics and dynamics of the vehicle itself. Control of the robotic manipulator's end-effector position is, therefore, more difficult than for the terrestrial manipulator and requires a robust control algorithm. One simple solution to this problem is to fix the vehicle to the surrounding environment. The robotic manipulator may then be controlled using typical control algorithms developed for fixed terrestrial manipulators. However, fixing the vehicle presents another set of problems, such as the requirement of a device for anchoring (such as another manipulator). Furthermore, the surrounding environment may not always provide adequate conditions for a safe and secure connection, as would be expected at sites of interest such as a hydrothermal vent.

Another solution is to decouple the vehicle and robotic manipulator by running an exclusive control loop to maintain a fixed vehicle position and orientation using the propulsion system, as studied in [25], [26], [31], [32], [34], [35], and [39]. For free-flying spacecraft, this would only be acceptable for fixing the orientation and not the position. Rotational control effort from reaction wheels or gyroscopes would be available, but translational control effort from propellant-driven thrusters would be too costly.

The problem addressed in work by Lapierre *et al.* [25], Fraisse *et al.* [26], Yuh [31], Yuh and Lakshmi [32], Tarn *et al.* [34], McLain *et al.* [35], and Koval [39] is improving station keeping of the vehicle during manipulator operation. Fraisse *et al.* investigate the use of force/torque sensors installed at the manipulator base for sensing and compensating for the reaction forces due to manipulator motion. Yuh and Lakshmi model the response of the combined vehicle–manipulator system using an artificial neural network learning algorithm in [31] and a parameter adaptation algorithm in [32], both of which estimate the model parameters to reduce manipulator end-effector error. Tarn *et al.* model the kinematics and dynamics of the manipulator including hydrodynamic effects to predict the compensation forces and moments required for station keeping of the vehicle. McLain *et al.* also model the kinematics and dynamics of the manipulator including hydrodynamic forces to improve station keeping of the vehicle. Koval similarly models the kinematics and dynamics of the manipulator for feedforward compensation of vehicle motion [39], but does not consider hydrodynamic forces. Improvements in vehicle station keeping using computer vision have also been studied by Leabourne *et al.* [40].

Control algorithms for vehicle–manipulator systems have also been investigated which allow for greater flexibility in the system by including vehicle motion within the manipulator trajectory control, such as by Antonelli *et al.* [41], [43]. Force control for manipulators is important when interacting with the environment, and has been studied by Yoerger *et al.* [42] and Antonelli *et al.* [44]. Vehicle motion may also be used to complement the capabilities of the manipulator by providing extra DOFs, as studied by Antonelli *et al.* [45]–[47].

For spacecraft-manipulator systems, it has been shown that the translational reactions of the vehicle may be allowed and compensated within the manipulator controller while the vehicle orientation is stabilized by its attitude control system [23]. This is an extension of previous work which also allows vehicle

motion but does not stabilize the vehicle orientation, such as [27] and [38]. Although a submersible may not be limited by a fixed amount of propellant, it may still be desirable to reduce the control effort of the propulsion system to conserve power, particularly if batteries are used as a primary power supply. This paper presents a strategy for coupled vehicle–manipulator control of an AUV system which reduces the energy consumption of the thruster control system used for station keeping.

The focus of this paper is the comparison of position and orientation stabilization during manipulator motion using combinations of feedback and feedforward control terms, with emphasis on improving efficiency by stabilization of the system barycenter instead of the vehicle itself. Manipulator motion is governed by a prescribed trajectory since the position control algorithm for driving the manipulator joints is not investigated. Instead, manipulator control is considered a separate problem in which either position stabilization of the vehicle body or system barycenter may be used. Control of the vehicle–manipulator system is simulated using a model with consideration of various hydrodynamic effects and environmental conditions. While the simulation results suggest the method successfully reduces the energy consumption of the system, subsequent experimental testing must still be performed for verification.

The resulting improvement in energy efficiency may be applied within any manipulator control algorithm simply by exchanging the vehicle position for the barycenter position as a reference point. Furthermore, the use of desired vehicle motion, as in [45]–[47], may still be employed by similarly changing the reference point from the vehicle position to the system barycenter. While the improvement in energy efficiency is crucial for implementation of vehicle–manipulator control on a spacecraft AUV exploring the oceanic environment of Europa, the algorithm may also be applied to terrestrial untethered AUV systems.

II. Mathematical Model

Modeling of the system is accomplished by considering the kinematics and dynamics of both the vehicle and the manipulator, including translation and rotation, as well as hydrodynamic effects such as drag and added mass. The model is extended to include the coupling effects and resulting vehicle–manipulator interaction behavior. Control inputs for the vehicle thruster system are determined using a simple control law which stabilizes the vehicle orientation and reference position. Furthermore, thruster dynamics are modeled to impose realistic control inputs during simulation.

A. Kinematics

Consider a robotic manipulator with N degrees of freedom, limited to revolute joints, and described using Denavit–Hartenberg parameters. Each link is represented by three vectors: link length l, link center of mass r, and link offset s. These vectors are defined with respect to the link coordinate system. The following equation describes the relationship between l, r, and s, where subscript i refers to the link index:

$$l_i = r_i + s_i. \tag{1}$$

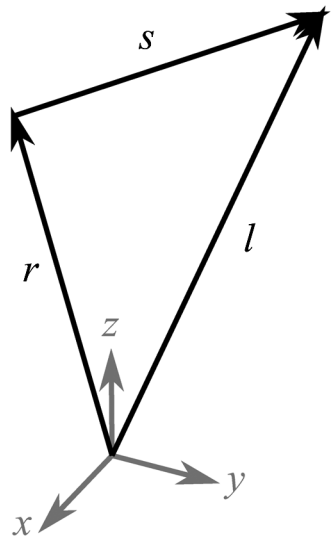

Fig. 2. Vectors r, s, and l with respect to the link coordinate system.

Fig. 2 shows the relationship between vectors r, s, and l.

The orientation of each link is given by rotation matrix R and the position of each link relative to the manipulator base p is defined by

$$p_i = \sum_{j=1}^{i} R_j l_j. \tag{2}$$

Accounting for vehicle position r_0, vehicle orientation R_0, and offset from the vehicle position to manipulator base s_0, the position of each link within inertial coordinates p^* is defined by

$$p_i^* = r_0 + R_0 s_0 + \sum_{j=1}^{i} R_j l_j. \tag{3}$$

Fig. 3 shows the relationship between the coordinate systems and position vectors, where O_I is the inertial reference coordinate system, O_0 is the vehicle coordinate system, O_B is the manipulator base coordinate system, O_i is the coordinate system of link i, O_{i-1} is the coordinate system of link $i-1$, and O_{cm} is the coordinate system of the system barycenter. Although the figure shows the vehicle and base coordinate systems aligned with the inertial reference frame, they will both have an orientation described by vehicle orientation matrix R_0.

It has been shown in [23] that the position of the end effector within inertial coordinates is defined by

$$p_N^* = p_{cm}^* + \left(1 - \frac{m_0}{m_T}\right) R_0 s_0 + \sum_{i=1}^{N} R_i \lambda_i - \frac{m_{N+1}}{m_T} R_{N+1} r_{N+1} \tag{4}$$

where m_0 is the mass of the vehicle, m_T is the total mass of the vehicle and the manipulator, and subscript $N+1$ refers to any payload carried by the end effector. The center of mass of the vehicle and the manipulator p_{cm}^* is defined by

$$p_{cm}^* = r_0^* + \left(1 - \frac{m_0}{m_T}\right) R_0 s_0 + \sum_{i=1}^{N} R_i L_i + \frac{m_{N+}}{m_T} R_{N+1} r_{N+1}. \tag{5}$$

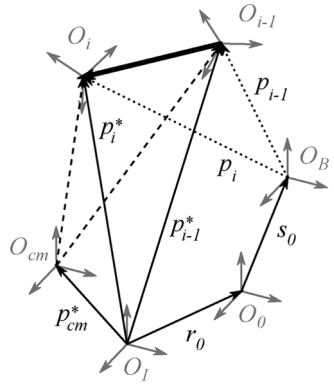

Fig. 3. Relationship between coordinate systems and position vectors of the vehicle and the manipulator.

The link length parameters λ and L are defined, respectively, by

$$\lambda_i = \frac{1}{m_T}\left[\left(\sum_{j=0}^{i} m_j l_j\right) - m_i r_i\right] \tag{6}$$

$$L_i = \frac{1}{m_T}\left[\left(\sum_{j=i+1}^{N+1} m_j l_j\right) + m_i r_i\right]. \tag{7}$$

Equation (4) defines the position of the end effector within inertial coordinates for a manipulator coupled to a free-floating vehicle. Assuming conservation of momentum applies, the center of mass of the entire system is static, therefore the first term is constant. For a vehicle with attitude stabilization, the vehicle orientation remains static, therefore the second term is also constant. The remaining terms represent a virtual manipulator whose link lengths are reduced but whose base is fixed within inertial coordinates. This results in the end-effector position decoupled from the vehicle position.

This approach allows the vehicle-mounted robotic manipulator to be treated as if it were fixed in inertial coordinates at the base and composed of shorter links. Translational motion of the vehicle due to reactions of the manipulator motion may be ignored, while attitude control actively stabilizes the orientation of the vehicle through feedforward control. Although conservation of momentum is not a valid assumption when the vehicle–manipulator system is immersed in fluid, this approach may still be employed if nonconservative effects are compensated.

III. Dynamics

The dynamics of the robotic manipulator coupled with the vehicle is analyzed using the Newton–Euler method. Computation of the angular and linear velocities and accelerations of each link center of mass is used to determine the inertial reaction forces and moments of each link. Using a backwards recursive process, the total force and moment on each link may be determined. Projection of the total moment onto the rotation axis of each link results in the joint torque. The total force and moment exerted upon the vehicle is converted to a feedforward signal for the attitude control system. The angular velocities ω of each link are determined from the angular velocities and accelerations of the joints, which are defined, respectively, by

$$\omega_i = \omega_{i-1} + z_i\dot{\theta}_i \tag{8}$$

$$\dot{\omega}_i = \dot{\omega}_{i-1} + z_i\ddot{\theta}_i + \omega_i \times z_i\dot{\theta}_i \tag{9}$$

where the rotation axis z is determined from the rotation matrix of each link using

$$z_0 = \begin{bmatrix} 0 \\ 0 \\ 1 \end{bmatrix} \tag{10}$$

$$z_i = R_{i-1} z_0. \tag{11}$$

The linear velocities v and accelerations of each link and its center of mass are determined from

$$v_i = v_{i-1} + \omega_i \times R_i l_i \tag{12}$$

$$\dot{v}_i = \dot{v}_{i-1} + \dot{\omega}_i \times R_i l_i + \omega_i \times (\omega_i \times R_i l_i) \tag{13}$$

$$v_{ci} = v_i + \omega_i \times -R_i s_i \tag{14}$$

$$\dot{v}_{ci} = \dot{v}_i + \dot{\omega}_i \times -R_i s_i + \omega_i \times (\omega_i \times -R_i s_i). \tag{15}$$

The inertial reaction forces and moments of each link are then computed, respectively, from

$$F_{ci} = m_i \dot{v}_{ci} \tag{16}$$

$$N_{ci} = I_i \dot{\omega}_i + \omega_i \times I_i \omega_i. \tag{17}$$

Since the forces and moments are computed within an inertial reference frame, the moment of inertia tensors must be updated according to the orientation of each body using

$$I_i = R_i I_{Bi} R_i^T. \tag{18}$$

Note that subscript B refers to the local reference frame of each body.

For a submersible vehicle, viscous drag must also be addressed. It is assumed that the viscous drag may be computed from

$$D_i = -\frac{1}{2}\rho C_{Di} A_i |w_i| w_i. \tag{19}$$

This quadratic drag law has been used in many similar research papers such as [29], and [34]–[37].

In (19), ρ is the fluid density, A_i is the link area, and w_i is the relative velocity of the link, as defined by

$$w_i = v_i - v_\infty \tag{20}$$

where v_∞ is the velocity of the surrounding fluid. The link area may be assumed to be the product of the link diameter d_L and link length.

The drag coefficient C_D is a function of the flow direction. Typical application of this drag formula assumes that the flow direction is defined by the angle of attack. Since the manipulator links may be traveling in any general direction, the dependency

upon flow direction is more complex. However, the effect of angle of attack may be approximated using

$$C_{Di} = C_{D0i} \sin^2 \alpha_i \tag{21}$$

$$\alpha_i = \cos^{-1}\left(\frac{z_{0i} \cdot w_i}{|w_i|}\right) \tag{22}$$

where α is the angle of attack, defined with respect to the longitudinal axis of each link as in (22) [34]. Moments due to rotational drag, as well as forces and moments due to lift are all neglected.

Net forces f and moments n acting upon each link are then determined using a backwards recursive process. The following equations define the forces and moments acting upon each link including inertia, gravity, buoyancy, and drag, as well as the reactions from the subsequent link:

$$\beta_i = \rho V_i \tag{23}$$

$$f_i = f_{i+1} + F_{ci} - m_i g + \beta_i g - D_i \tag{24}$$

$$\begin{aligned} n_i = {} & n_{i+1} + N_{ci} + R_i l_i \times f_{i+1} + R_i r_i \times F_{ci} \\ & + R_i r_i \times -m_i g + R_i \mu_i \times \beta_i g + R_i \eta_i \times -D_i \end{aligned} \tag{25}$$

where β is the mass of displaced fluid, V is the link volume, and μ and η are the vector locations of the center of buoyancy and aerodynamic center of the link in its local reference frame, respectively.

Another important consideration is the phenomenon of added mass. For fluids with low density, drag is the dominant resisting force of the fluid upon a moving body. However, higher density fluids impose additional resistance when a moving body accelerates since the fluid around the body must also be accelerated [33]. The resisting forces and moments due to translational and rotational accelerations are determined by the relationship in

$$\begin{bmatrix} F_x \\ F_y \\ F_z \\ N_x \\ N_y \\ N_z \end{bmatrix} = \rho M_a \begin{bmatrix} \dot{v}_x \\ \dot{v}_y \\ \dot{v}_z \\ \dot{\omega}_x \\ \dot{\omega}_y \\ \dot{\omega}_z \end{bmatrix} \tag{26}$$

where M_a is the added mass coefficient matrix.

For a sphere, the off-diagonal terms of M_a are zero and there are no coupled effects between the various axes of motion due to symmetry. However, if the body shape is asymmetric, then there will be nonzero off-diagonal terms such that a translational or rotational acceleration along one axis will cause forces and moments along different axes. Modeling the added mass coefficients requires detailed analysis of the link geometry. To include the coupled effects of added mass without performing this detailed analysis, it is assumed that each link has the same set of added mass coefficients but scaled according to the link volume. Therefore, the added mass matrix for link i, M_{ai}, is given by

$$M_{ai} = V_i M_a^0 \tag{27}$$

where M_{a0} is the unscaled matrix of added mass coefficients. The added mass matrix for the vehicle body is determined similarly using the vehicle volume.

A. Perturbations

Computation of the hydrodynamic effects upon the manipulator and vehicle requires knowledge of the velocity of the surrounding fluid v_∞. While it is assumed that the fluid velocity is constant and estimated by the vehicle, it is likely that there will be perturbations due to the unsteady nature of fluid in an ocean. Therefore, the actual fluid velocity is modeled as the superposition of a steady component and an unsteady component, with the latter modeled using a time-dependent Fourier series. The actual fluid velocity is given by

$$v_\infty = v_\infty^0 + A_v \sum_{i=1}^{n} \left(\frac{\Psi_{si}}{i} \sin\left(2\pi i \frac{t}{t_F}\right) + \frac{\Psi_{ci}}{i} \cos\left(2\pi i \frac{t}{t_F}\right) \right) \tag{28}$$

where v_∞^0 is the steady component and A_v is the amplitude of the unsteady component, which is composed of n harmonic terms whose coefficients Ψ_{si} and Ψ_{ci} are random values between -1 and 1. Note that the actual fluid velocity is used to compute the simulated hydrodynamic effects imposed upon the manipulator and vehicle, while only the steady component is used to compute the modeled hydrodynamic effects for feedforward control.

B. Vehicle Control

The joint torques are computed from the projection of the net moment n, upon the joint axis z. The following equation defines the joint torque, where damping and elasticity in the joint are neglected:

$$\tau_i = n_i \cdot z_i. \tag{29}$$

The net force and moment upon the manipulator base may then be used to determine the net moment upon the vehicle center of mass. A feedforward signal may then be provided to the attitude control system to balance the net moment and provide attitude stabilization [27]. The following equation defines the feedforward torque required for vehicle stabilization N_r:

$$N_r = n_1 - (p_{cm}^* - r_0 - R_0 s_0). \tag{30}$$

Similarly, in the case that dedicated vehicle position stabilization is desired, a feedforward force signal is necessary for the propulsion system. The following equation defines the feedforward force required for vehicle stabilization $F_{r,0}$, where D_0 is the drag acting on the vehicle body and f_1 is the net reaction force at the manipulator base:

$$F_{r,0} = f_1 - D_0. \tag{31}$$

However, it may be desired to conserve power and reduce controller effort by neglecting the reaction forces due to manipulator motion since they are conservative and holonomic. In such a case, the resulting forces upon the vehicle are simply the drag, gravity, and buoyancy forces acting on both the manipulator and the vehicle. Ideally, this case mimics the system acting freely in space with no surrounding fluid. The feedforward control force, therefore, maintains the system center of mass at a static location. Note that it is assumed that attitude stabilization

TABLE I
FEEDFORWARD CONTROL FORCES

Case	Feedforward Control Force, F_r
Vehicle Stabilization	$F_{r,0}$
Barycenter Stabilization	$F_{r,cm}$

is also active. The following equation defines the feedforward force required for barycenter stabilization, $F_{r,cm}$:

$$F_{r,cm} = \sum_{i=0}^{N+1} \left(-D_i - m_i g + \beta_i g\right). \tag{32}$$

Therefore, either the vehicle position or system barycenter may be stabilized by using either $F_{r,0}$ or $F_{r,cm}$ as the feedforward control force signal F_r. This is summarized in Table I.

It is important to note that the dynamic model is used both for the onboard vehicle controller model (the predictive model that would be applied for experimental validation) as well as for the simulation of the actual dynamic effects during motion. Without any imposed differences between the actual and model parameters, the modeled and simulated dynamics will match and, therefore, compensation of the manipulator reactions will always be perfect with the exception of the unknown fluid flow defined by (28). Further improvements in the modeling of hydrodynamic effects could be made (particularly distributed drag and added mass along each manipulator link as analyzed in [35]–[37]), but differences would only be seen during experimental validation, where the simulated response is replaced with the true response. Further research could be conducted in the future to augment the hydrodynamic model as such. Consider a vehicle driven by a set of M propellers, each located at a position a, with respect to the vehicle center of mass, and producing a force P, with direction vector u, with respect to the vehicle coordinate system. The net forces and moments due to the propeller thrust values are determined using the transformation defined by

$$\begin{bmatrix} F_{PB} \\ N_{PB} \end{bmatrix} = HP \tag{33}$$

where P is the vector of propeller thrust values, F_{PB} is the net force vector, and N_{PB} is the net moment vector. Note that F_{PB} and N_{PB} act at the vehicle center of mass and with respect to the vehicle coordinate frame. The transformation matrix H is defined by

$$H = \begin{bmatrix} u_1 & u_2 & \dots & u_M \\ a_1 \times u_1 & a_2 \times u_2 & \dots & a_M \times u_M \end{bmatrix}. \tag{34}$$

Since the propellers are defined with respect to the vehicle body frame of reference, the net forces and moments with respect to the inertial frame of reference must be determined from the vehicle orientation R_0. This is accomplished using the transformation defined by

$$\begin{bmatrix} F_{P0} \\ N_{P0} \end{bmatrix} = \begin{bmatrix} R_0 & 0 \\ 0 & R_0 \end{bmatrix} \begin{bmatrix} F_{PB} \\ N_{PB} \end{bmatrix} \tag{35}$$

where F_{P0} and N_{P0} are the vectors of forces and moments with respect to inertial coordinates. Substitution of (33) yields

$$\begin{bmatrix} F_{P0} \\ N_{P0} \end{bmatrix} = \begin{bmatrix} R_0 & 0 \\ 0 & R_0 \end{bmatrix} HP \tag{36}$$

which defines the net force and moment upon the vehicle due to propeller thrust.

The control system must determine the necessary thrust for each propeller to provide a desired set of forces and moments upon the vehicle body. The vector of propeller thrust values may be determined from the net force and moment by rearranging (36), as given by

$$P = H^{-1} \begin{bmatrix} R_0^T & 0 \\ 0 & R_0^T \end{bmatrix} \begin{bmatrix} F_{P0} \\ N_{P0} \end{bmatrix} \tag{37}$$

However, this requires inversion of H, which is only possible for a vehicle with six propellers, where H is square.

Six is the minimum number of propellers required to ensure controllability of the vehicle in both translation and rotation. However, there may be fewer or more propellers which cause H to be nonsquare. In such a case, matrix H must be inverted using a pseudoinverse H^+, defined by

$$H^+ = H^T (H H^T)^{-1}. \tag{38}$$

The propeller thrust values required to produce the desired forces and moments upon the vehicle may then be determined by

$$P = H^+ \begin{bmatrix} R_0^T & 0 \\ 0 & R_0^T \end{bmatrix} \begin{bmatrix} F_{P0} \\ N_{P0} \end{bmatrix}. \tag{39}$$

Stabilization of the vehicle orientation is accomplished using the feedforward moments from the robotic manipulator control system combined with a conventional PD feedback controller. The following equation defines the feedback control torque:

$$N_{fb} = K_{PN} \phi e - K_{DN} \omega_0 \tag{40}$$

while

$$N_{P0} = N_{fb} + N_r \tag{41}$$

defines the net desired control torque due to both feedback and feedforward terms, where K_{PN} and K_{DN} are the proportional and derivative gains of the feedback controller, respectively, ϕ is the orientation error rotation angle, and e is the orientation error rotation axis. The orientation error is defined using Euler's axis-angle theorem, defined by

$$\phi = \cos^{-1}\left(\frac{E_{11} + E_{22} + E_{33} - 1}{2}\right) \tag{42}$$

$$e = \frac{1}{2\sin\phi} \begin{bmatrix} E_{32} - E_{23} \\ E_{13} - E_{31} \\ E_{21} - E_{12} \end{bmatrix}. \tag{43}$$

Error rotation matrix E represents the transformation from current vehicle orientation R_0 to the desired vehicle orientation R_{0d}. The following equation defines the error rotation matrix:

$$E = R_{0d} R_0^T. \tag{44}$$

Similarly, control of the vehicle position may be accomplished with a combination of feedback and feedforward terms. The following equation defines the feedback control force:

$$F_{fb} = K_{PF}(r_{0d} - r_0) + K_{DF}(v_{0d} - v_0) \tag{45}$$

while

$$F_{P0} = F_{fb} + F_r \tag{46}$$

defines the net desired control force including both feedback and feedforward terms, where the desired position and velocity are r_{0d} and v_{0d}, respectively, and the proportional and derivative gains are K_{PF} and K_{DF}, respectively.

As previously discussed, the feedforward control term may be for either vehicle stabilization or barycenter stabilization. In the case of barycenter stabilization, the feedback term serves to minimize the error in the barycenter position instead of the vehicle position. The case of vehicle stabilization may also be investigated using feedback control alone by neglecting the feedforward control term.

C. Thruster Control

A separate control system varies the propeller motor speed and torque to achieve the desired propeller thrust requested by the AUV control system. Each propeller is treated independently. Propeller thrust T and torque Q are functions of the propeller shaft speed ω_m, where ρ is the fluid density, D is the propeller diameter, and K_T and K_Q are the thrust and torque coefficients, respectively. The thrust and torque are defined by (as in [28])

$$T = \frac{K_T \rho D^4 \omega_m^2}{4\pi^2} \text{sign}(\omega_m) \tag{47}$$

$$Q = \frac{K_T \rho D^5 \omega_m^2}{4\pi^2} \text{sign}(\omega_m). \tag{48}$$

The thrust and torque coefficients are a function of the advance ratio ζ, which is the ratio of the relative velocity of the fluid with respect to the vehicle (along the direction of the thruster) to the propeller tip speed. The following equation defines the advance ratio:

$$\zeta = \frac{2\pi v_a}{\omega_m D} \tag{49}$$

where the advance speed v_a is defined by

$$v_a = u \cdot (v_0 - v_\infty). \tag{50}$$

The following equations define the thrust and torque coefficients, respectively:

$$K_T = C_{T1}\zeta + C_{T2} \tag{51}$$

$$K_Q = C_{Q1}\zeta + C_{Q2}. \tag{52}$$

It may be assumed that the coefficients are linear functions of the advance ratio, with slopes C_{T1} and C_{Q1}, and offsets C_{T2} and C_{Q2}.

The propeller is driven by an electric motor attached to a shaft, where no gear reduction is assumed. The equation of motion for the motor is defined by

$$V = R_m I + L_m \dot{I} + k_m \omega_m \tag{53}$$

where V and I are the motor voltage and current, respectively, and R_m and L_m are the motor resistance and inductance, respectively.

The following equation defines motor torque τ, where k_m is the motor constant:

$$\tau = k_m I. \tag{54}$$

The equation of motion for the shaft with propeller and motor attached is defined by

$$J\dot{\omega}_m + b\omega_m = \tau - Q \tag{55}$$

where J is the shaft moment of inertia, and b is the viscous damping of the shaft.

Control of the vehicle is accomplished by first determining the desired thrust for each propeller. Since the thrust is a function of the propeller speed, the desired propeller speed may be determined from the desired thrust. Substitution of (49) into (47) yields

$$0 = \frac{C_{T2}\rho D^4}{4\pi^2}\hat{\omega}_m^2 + \frac{C_{T1} v_a \rho D^3}{2\pi}\hat{\omega} - \hat{T}. \tag{56}$$

Note that the hat operators above ω and T indicate desired values.

Solution of this quadratic equation results in the required propeller speed necessary to achieve a desired thrust. However, it is necessary to take the absolute value of the desired thrust to avoid complex solutions. Furthermore, it is found that the two solutions to the quadratic equation represent the desired propeller speed for positive and negative thrust. This algorithm is described by

$$0 = c_1\hat{\omega}_m^2 + c_2\hat{\omega} + c_3 \tag{57}$$

$$c_1 = \frac{C_{T2}\rho D^4}{4\pi^2} \tag{58}$$

$$c_2 = \frac{C_{T1} v_a \rho D^3}{2\pi} \tag{59}$$

$$c_3 = |T| \tag{60}$$

$$\hat{\omega}_{m+} = \frac{-c_2 + \sqrt{c_2^2 - 4c_1c_3}}{2c_1} \tag{61}$$

$$\hat{\omega}_{m-} = \frac{-c_2 - \sqrt{c_2^2 - 4c_1c_3}}{2c_1} \tag{62}$$

$$\hat{\omega}_m = \begin{cases} \hat{\omega}_{m+}, & \hat{T} \geq 0 \\ \hat{\omega}_{m-}, & \hat{T} < 0. \end{cases} \tag{63}$$

A simple proportional control law is used to determine the desired propeller acceleration. The control law is defined by

$$\dot{\hat{\omega}}_m = K_A(\hat{\omega}_m - \omega_m) \tag{64}$$

where K_A is the gain.

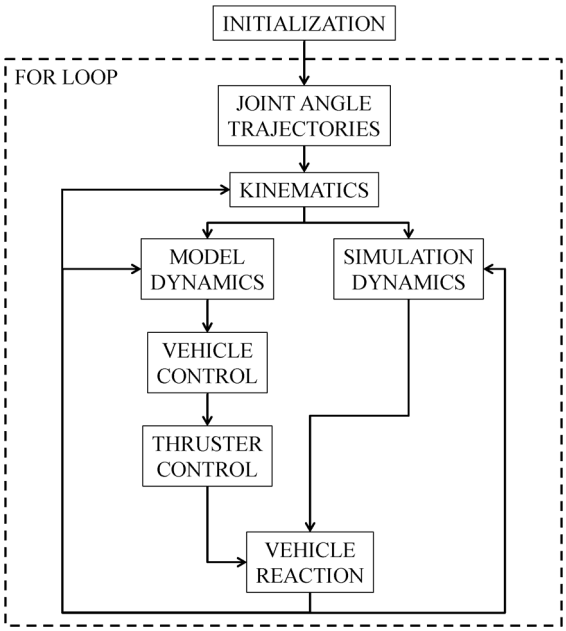

Fig. 4. Simulation flow chart.

Fig. 5. Barrett WAM manipulator.

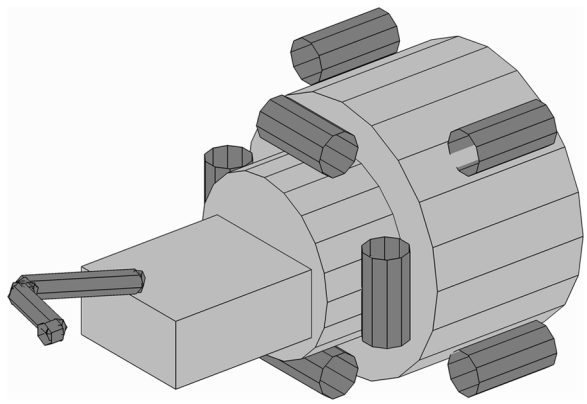

Fig. 6. Model of the AUV vehicle–manipulator system.

The desired motor current is determined by combining (54) and (55) and substituting the desired propeller acceleration and actual propeller speed. Furthermore, the propeller torque is evaluated with the actual propeller speed. The following equation defines the desired motor current:

$$\hat{I} = \frac{J\dot{\hat{\omega}}_m + b\omega_m + Q}{k_m}. \tag{65}$$

Similarly, another simple proportional control law is used to determine the desired rate of change of motor current. The following equation defines the rate of change of the motor current, where K_B is the gain:

$$\dot{I} = K_B(\hat{I} - I). \tag{66}$$

Equation (63) is integrated to determine the motor current. The required motor voltage is then determined from (53). It is assumed that the power supply response time is negligible. The actual propeller acceleration is then determined from the combination of (54) and (55) which yields

$$\dot{\omega}_m = \frac{k_m I - b\omega_m - Q}{J}. \tag{67}$$

The propeller speed is then determined by integration of (67). The actual thrust and torque produced by the propeller are then determined from the propeller speed using (47) and (48).

IV. Simulation

The kinematics and dynamics of the AUV vehicle and manipulator system are modeled and simulated in MATLAB. The purpose of the simulation is to compare the performance of the manipulator with barycenter stabilization and with vehicle position stabilization, as well as verify the performance of the vehicle and thruster control system. The simulation is run as outlined in the flow diagram shown in Fig. 4. Initialization consists of the setup of parameters and computation of the link length parameters λ and L, and added mass matrices. The joint angles, velocities, and accelerations are evaluated within each iteration of the for-loop. The kinematics and dynamics of the manipulator are then computed. Actual fluid density and unsteady flow are considered in the simulation dynamics, while estimated fluid density and no unsteady flow are used for the model dynamics. The vehicle control algorithm then determines the necessary control inputs, which are passed to the thruster control algorithm. The result then determines the actual control inputs, and the vehicle reaction is computed. The vehicle reaction also feeds back into the kinematics, dynamics, and vehicle control algorithms.

A. System Description

The system modeled for simulation is composed of a 7-DOF robotic manipulator coupled to a simple AUV with eight thrusters. The manipulator is modeled after the Barrett whole

TABLE II
MANIPULATOR LINK AND DH PARAMETERS

Link, i	Mass, m_{Bi} (kg)	DH Parameters		
		α_i(rad)	a_i(mm)	d_i(mm)
1	10.77	$-\frac{\pi}{2}$	0	0
2	3.87	$\frac{\pi}{2}$	0	0
3	1.80	$-\frac{\pi}{2}$	45	550
4	2.40	$\frac{\pi}{2}$	-45	0
5	0.12	$-\frac{\pi}{2}$	0	300
6	0.42	$\frac{\pi}{2}$	0	0
7	0.07	0	0	60

TABLE III
MANIPULATOR LINK CENTER OF MASS LOCATIONS

Link, i	Center of Mass, r_i (mm)		
	$r_{i,x}$	$r_{i,y}$	$r_{i,z}$
1	-4.4	121.9	-0.7
2	-2.4	31.1	15.4
3	6.7	-342.5	0.0
4	-40.0	-0.2	132.7
5	0.1	-294.9	4.4
6	-0.1	-17.0	24.7
7	-0.1	0.2	56.8

TABLE IV
LINK MOMENT OF INERTIA TERMS

Link, i	Moment of Inertia I_{Bi} (kg $\cdot$ m^2)		
	$I_{Bi,xx}$	$I_{Bi,yy}$	$I_{Bi,zz}$
1	0.1349	0.1133	0.0905
2	0.0214	0.0138	0.0156
3	0.0591	0.0032	0.0593
4	0.0149	0.0148	0.0029
5	0.0001	0.0001	0.0001
6	0.0006	0.0002	0.0004
7	0.0000	0.0000	0.0001

arm manipulator (WAM), while the AUV resembles the configuration of the University of Maryland Ranger NBV. The Barrett WAM, shown in Fig. 5, is a popular robotic manipulator for research due to its smooth motion, backdrivability, and low power consumption [30]. Although the Barrett WAM is not designed for use on an AUV, its kinematic and dynamic parameters are used for this simulation. The AUV model is shown in Fig. 6.

Tables II–V list the parameters of the robotic manipulator, vehicle, and environment, as well as additional simulation parameters.

TABLE V
LINK, VEHICLE, AND ENVIRONMENT PARAMETERS

Link Diameter, d_L (mm)		89
Link Drag Coefficient, C_{DL0}		1.0
Vehicle Mass, m_{B0} (kg)		120
Vehicle Area, A_0 (m^2)		0.5
Vehicle Volume, V_0 (m^3)		0.15
Payload Mass, m_{N+1} (kg)		10
Fluid Density, $\rho(\frac{\text{kg}}{\text{m}^3})$		1025
Manipulator Offset, (m)	$s_{0,x}$	0.914
	$s_{0,y}$	0
	$s_{0,z}$	0.152
Fluid Velocity , (m/s)	$v_{\infty,x}$	0
	$v_{\infty,y}$	0
	$v_{\infty,z}$	0

TABLE VI
THRUSTER CONFIGURATION PARAMETERS

Thruster, j	Position, a_j			Direction, u_j		
	$a_{j,x}$	$a_{j,y}$	$a_{j,z}$	$u_{j,x}$	$u_{j,y}$	$u_{j,z}$
1	-0.5	0.5	0.5	1	0	0
2	-0.5	-0.5	0.5	1	0	0
3	-0.5	0.5	-0.5	1	0	0
4	-0.5	-0.5	-0.5	1	0	0
5	0.1	0.5	0	0	0	1
6	0.1	-0.5	0	0	0	1
7	0.1	0	0.5	0	1	0
8	0.1	0	-0.5	0	1	0

TABLE VII
MOTOR PARAMETERS

Motor Resistance, R_m (Ω)	1
Motor Inductance, L_m ($\Omega \cdot$ s)	1
Motor Constant, k_m (Nm/A)	10
Motor Damping, b (N $\cdot$ m $\cdot$ s)	0.01
Motor Inertia, J (kg $\cdot$ m^2)	0.01

The unscaled added mass matrix is given by

$$M_a^0 = \begin{bmatrix} 0.1 & 0 & 0 & 0 & 0 & 0 \\ 0 & 0.1 & -0.01 & 0 & 0 & 0 \\ 0 & -0.01 & 0.1 & 0 & -0.001 & 0 \\ 0 & 0 & 0 & 0.01 & 0 & 0.001 \\ 0 & 0 & -0.001 & 0 & 0.01 & 0 \\ 0 & 0 & 0 & 0.001 & 0 & 0.01 \end{bmatrix}. \tag{68}$$

Table VI lists the thruster configuration parameters, while Table VII lists the motor parameters.

Table VIII lists propeller parameters and simulation parameters as well as control parameters for both position and attitude control systems.

TABLE VIII
PROPELLER, CONTROL, AND SIMULATION PARAMETERS

Propeller Diameter (m)		0.05
Speed Control Gain, A		5
Current Control Gain, B		5
Simulation Duration (s)		60
Simulation Time Step (s)		0.03
Propeller Coefficients	C_{T1}	0.5
	C_{T2}	-0.5
	C_{Q1}	0.15
	C_{Q2}	-0.15
Position Feedback Gains	K_{PF}	10
	K_{DF}	100
Attitude Feedback Gains	K_{PN}	10
	K_{DN}	100

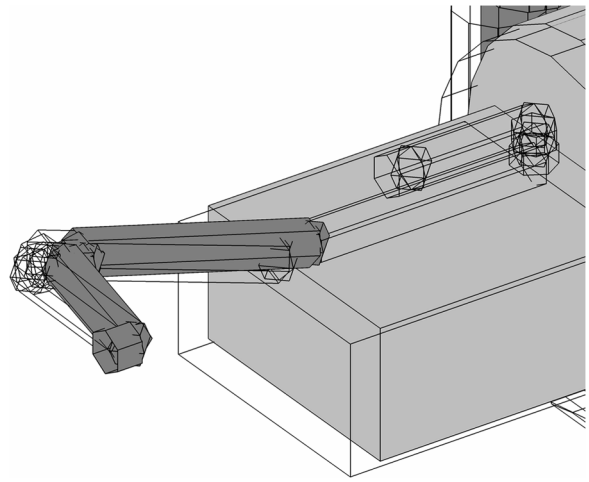

Fig. 7. Final configurations of the manipulator for vehicle position stabilization (wireframe) and barycenter stabilization. Note that the initial stowed configuration is shown in wireframe as well.

B. Trajectory

Manipulator motion is driven by a set of prescribed joint angle trajectories. Each joint moves independently from an initial angle to a final angle with continuous smooth motion. The trajectories are modeled using

$$\theta_i = \frac{(\theta_{Fi} - \theta_{Ii})}{2\pi} \sin\left(2\pi \frac{t}{t_F}\right) + (\theta_{Fi} - \theta_{Ii}) \frac{t}{t_F} \theta_{Ii} \tag{69}$$

$$\dot{\theta}_i = \frac{(\theta_{Fi} - \theta_{Ii})}{t_F} \cos\left(2\pi \frac{t}{t_F}\right) + \frac{(\theta_{Fi} - \theta_{Ii})}{t_F} \tag{70}$$

$$\ddot{\theta}_i = 2\pi \frac{(\theta_{Fi} - \theta_{Ii})}{t_F^2} \sin\left(2\pi \frac{t}{t_F}\right) \tag{71}$$

where θ_I and θ_F are the initial and final angles, respectively, and t_F is the length of the simulation.

The joint angle trajectories defined by (69)–(71) provide the necessary inputs for computing the kinematics and dynamics of the manipulator. However, as long as the joint angles, rates, and accelerations are known, any trajectory or manipulator control algorithm may be used. During simulation, the manipulator moves from an initial stowed configuration to a set of joint angles which position the end effector at a desired location in the inertial reference frame. The set of joint angles which position the end effector at that location will be different depending upon the use of vehicle position stabilization or barycenter stabilization since vehicle motion will occur in the latter. For barycenter stabilization, the amount of vehicle motion depends upon the payload mass. Therefore, the set of joint angles necessary to reach the desired end-effector position will depend upon the payload mass as well. Table IX lists the initial and final joint angles which define the trajectory for vehicle position stabilization and barycenter stabilization with various payload masses. The final joint angle configuration places the end effector at a position of (2.428, 0.250, 0.404 m) with respect to the inertial reference frame.

Fig. 7 shows the manipulator in the stowed configuration as well as reaching the final end-effector position for both vehicle position stabilization and barycenter stabilization.

Eight different scenarios are considered for the vehicle control system, as shown in Table X. To compare the performance of the controller, the end-effector error ε is defined as the difference between the actual end-effector position and the estimated end-effector position. For cases II, III, VII, and VIII, the estimated end-effector position is defined by (4), where the reference point is the system barycenter. For cases I, IV, V, and VI, the estimated end-effector position is defined by (3), where the reference point is the vehicle center of mass. It should be noted that attitude control for all cases employs both feedback and feedforward terms. All eight cases are simulated under two different sets of conditions. The first set of simulations are carried out assuming that the density of the fluid is known precisely and that the surrounding fluid is completely stagnant with no unknown currents. The second set of simulations are performed with a difference between the actual and modeled fluid density as well as including unknown unsteady currents, as defined by (28).

C. Results

Case I is the uncontrolled case in which the vehicle translates and rotates freely in reaction to manipulator motion. This case demonstrates the error at the manipulator end effector if the base were assumed to be fixed. Case II represents the control scheme for barycenter stabilization of a spacecraft–manipulator system with no compensation for hydrodynamic effects, hence assuming conservation of momentum applies. The orientation is stabilized and the end-effector position is known from (4). Case III is the feedforward barycenter stabilization case for the AUV–manipulator system. The orientation is stabilized and hydrodynamic effects are compensated through feedforward control only. The end-effector position is known from (4) where the barycenter is assumed fixed. Cases IV, V, and VI are all vehicle stabilization cases for the AUV–manipulator system. Feedback and feedforward control is employed for case IV while only feedback control is employed for case V and only feedforward control is employed for case VI. Since the vehicle position and orientation are stabilized, the manipulator is effectively fixed

TABLE IX
INITIAL AND FINAL JOINT ANGLES

Joint, i	θ_{Ii} (°)	θ_{Fi} (°)					
		Veh.	Bary. (0kg)	Bary. (1kg)	Bary. (2kg)	Bary. (5kg)	Bary. (10kg)
1	180	169.68	170.06	170.32	170.59	171.48	176.19
2	90	-75.62	-76.01	-76.12	-76.24	-76.58	-77.12
3	180	266.00	265.62	265.53	265.45	265.17	264.65
4	180	108.77	102.87	101.58	100.28	96.30	89.32
5	0	193.47	192.96	192.86	192.76	192.51	192.22
6	0	96.97	91.56	90.56	89.56	86.53	81.35
7	0	98.33	97.24	97.02	96.80	96.14	95.12

TABLE X
SIMULATION CONTROL SCENARIOS

Case	Attitude Control	Position Control		
		Reference	Feedforward	Feedback
I	No	Vehicle	No	No
II	Yes	Barycenter	No	No
III	Yes	Barycenter	Yes	No
IV	Yes	Vehicle	Yes	Yes
V	Yes	Vehicle	No	Yes
VI	Yes	Vehicle	Yes	No
VII	Yes	Barycenter	Yes	Yes
VIII	Yes	Barycenter	No	Yes

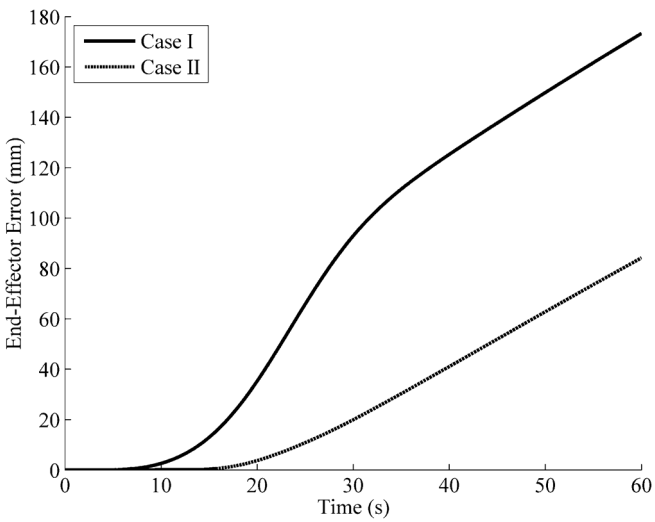

Fig. 8. End-effector position error for cases I (no control) and II (no hydrodynamic compensation), under stagnant conditions with no modeled density error.

in inertial coordinates. Therefore, the end-effector position is known from (3). Cases VII and VIII are both barycenter stabilization scenarios, where feedback and feedforward control are employed for case VII, but only feedback control is used for case VIII. The location of the barycenter is determined from (5) and updated at each time step.

1) Stagnant Conditions: The first set of simulations are performed with stagnant conditions and without any difference between the estimated and actual fluid density. Figs. 8–10 show the end-effector position error throughout the simulation for each of the eight cases under these conditions. The mean error and energy consumed are summarized in Table XI.

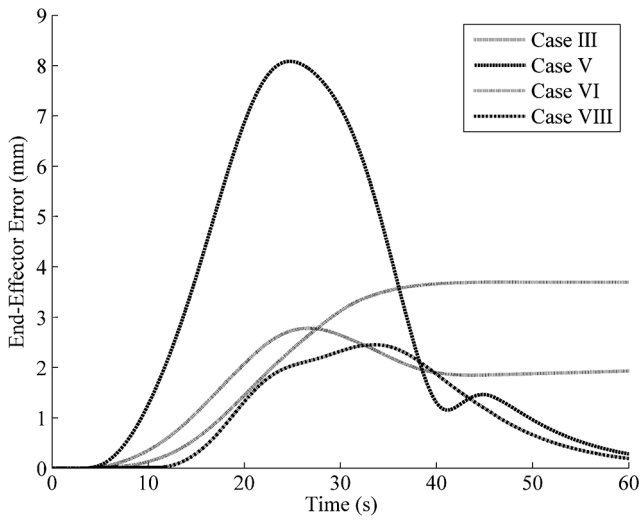

Fig. 9. End-effector position error for cases III (barycenter feedforward only), V (vehicle feedback only), VI (vehicle feedforward only), and VIII (barycenter feedback only) under stagnant conditions with no modeled density error.

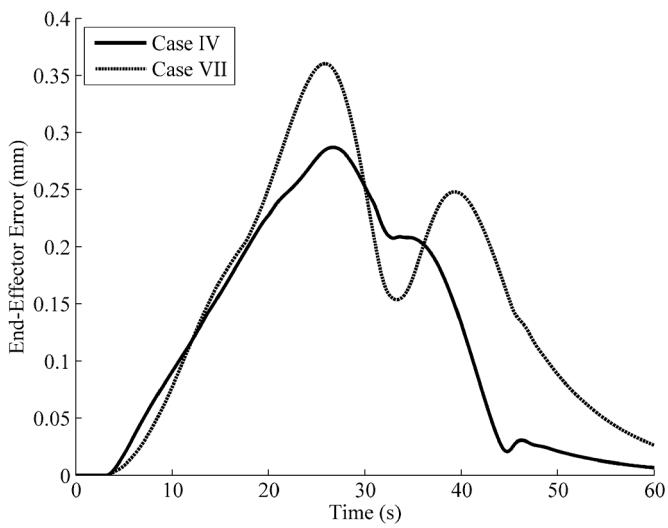

Fig. 10. End-effector position error for cases IV (vehicle feedforward and feedback) and VII (barycenter feedforward and feedback) under stagnant conditions with no modeled density error.

Case I resulted in the highest error, due to the uncompensated motion of the vehicle. Case II resulted in lower error, which is expected since the attitude control maintains a stable vehicle orientation. However, it can be seen that the error continues to

TABLE XI
END-EFFECTOR ERROR AND ENERGY CONSUMPTION (STAGNANT CONDITIONS)

Case	Mean End-Effector Error (mm)	Energy Consumed (J)
I	78.01	0
II	24.35	0.1807
III	1.85	0.1930
IV	0.12	0.3391
V	2.93	0.3523
VI	1.51	0.3326
VII	0.13	0.1946
VIII	0.91	0.1932

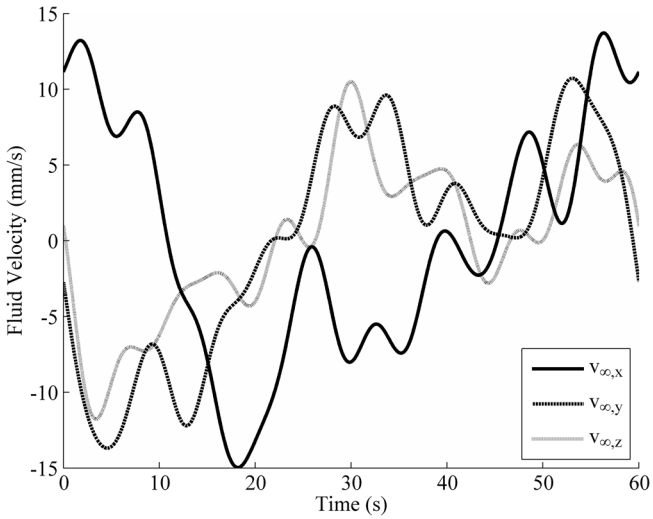

Fig. 11. Velocity of surrounding fluid.

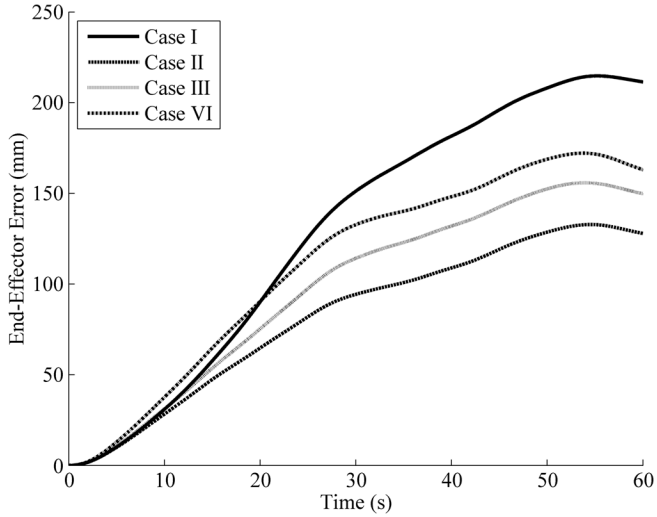

Fig. 12. End-effector position error for cases I (uncontrolled), II (no hydrodynamic compensation), III (barycenter feedforward only), and VI (vehicle feedforward only) with unsteady flow and fluid density error.

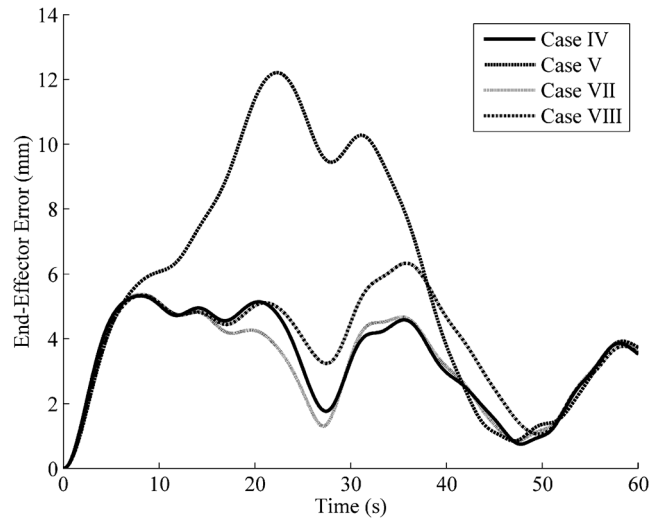

Fig. 13. End-effector position error for cases IV (vehicle feedforward and feedback), V (vehicle feedback only), VII (barycenter feedforward and feedback), and VIII (barycenter feedback only) with unsteady flow and fluid density error.

increase even after the manipulator has completed its trajectory. This is due to the nonconservative hydrodynamic effects, which are uncompensated. Cases III and VI resulted in much lower errors on average, but resulted in a steady-state error at the end of the manipulator motion. This is because both of these cases employed only feedforward control, and the slight motion of the reference point (the barycenter for case III and the vehicle for case VI) is uncompensated. Cases V and VIII also resulted in much lower errors on average as well as at the end of the trajectory. Both of these cases employ only feedback control. It can be seen that the errors during motion are much higher for the vehicle stabilization case without feedforward compensation. Cases IV and VII demonstrated the lowest end-effector position errors due to the combination of both feedback and feedforward control. Under stagnant conditions and assuming the fluid density is known exactly, the cases in which the barycenter was stabilized consumed on average approximately 43.3% less energy than the cases in which the vehicle position was stabilized. Note that the energy consumed is computed by integrating the product of the motor voltage and current. While the end-effector errors appear to be unrealistically small for a manipulator attached to a free-floating vehicle, it is important to note that the hydrodynamic effects are modeled for both simulation and control using the same equations. As mentioned previously, there will only be significant errors if the simulated dynamics can be replaced with a more accurate analysis of the true hydrodynamic effects. However, any improvements in the hydrodynamic model, such as in [35]–[37], would be applied to both vehicle control and simulation.

2) Perturbed Conditions: The second set of simulations are performed with more realistic conditions, including both unknown unsteady fluid flow and a difference between the modeled and actual fluid densities. Unsteady fluid flow is modeled using (28), resulting in the velocity profile shown in Fig. 11. Actual and model fluid densities are 1025 and 1000 kg/m^3, respectively, representing the effect of unknown salinity conditions. Figs. 12 and 13 show the end-effector position error throughout the simulation for each of the eight cases under these conditions. The mean error and energy consumed are summarized in Table XII.

It can be seen in Fig. 12 that cases I, II, III, and VI all result in large end-effector position errors due to the lack of feedback control, which is necessary, given the unknown external perturbations from unsteady flow and fluid density error. Fig. 13

TABLE XII
END-EFFECTOR ERROR AND ENERGY CONSUMPTION (UNSTEADY CONDITIONS)

Case	Mean End-Effector Error (mm)	Energy Consumed (J)
I	124.90	0
II	79.03	0.1839
III	95.90	0.1933
IV	3.32	0.6194
V	5.65	0.6087
VI	108.92	0.3259
VII	3.16	0.3871
VIII	3.70	0.3760

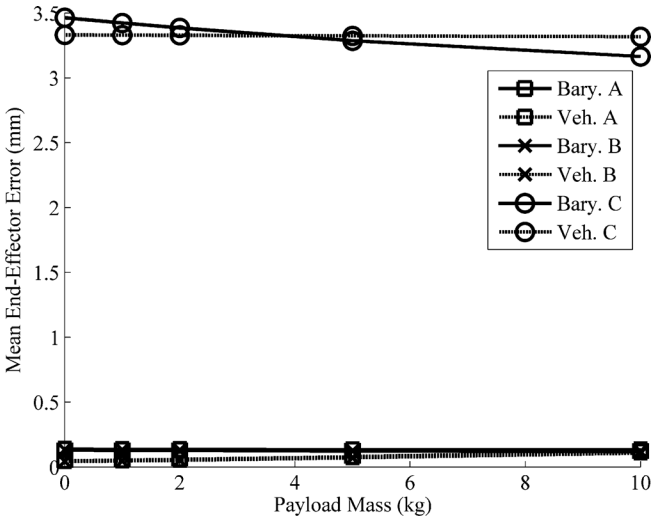

Fig. 14. End-effector error for various payload masses with (A) stagnant conditions with no density error; (B) stagnant conditions with density error; and (C) unsteady flow conditions with density error.

shows that cases IV, V, VII, and VIII all result in much lower end-effector position errors since feedback control is employed. Again, the error is much larger for the vehicle stabilization case without feedforward compensation. Considering only the cases with feedback control included, stabilization of the barycenter consumed on average 38.5% less energy than stabilization of the vehicle position when unsteady flow and fluid density error are included.

3) Influence of Payload Mass: Another important consideration is the effect of the payload mass upon the performance of the controller. Larger payloads will cause greater reactions at the manipulator base, therefore requiring greater propeller thrust during vehicle stabilization and imposing larger vehicle motion during barycenter stabilization. Three scenarios are considered: A) stagnant conditions with no density error; B) stagnant conditions with density error; and C) unsteady flow conditions with density error. The end-effector errors and amount of energy consumed for various payload masses using vehicle stabilization and barycenter stabilization (each with both feedback and feedforward control) are analyzed and shown in Figs. 14 and 15.

It can be seen in Fig. 14 that the mean end-effector error is only slightly affected by the mass of the payload, and is similar for both vehicle stabilization and barycenter stabilization in all three scenarios. There is a decrease in the mean end-effector error which is attributed to the higher inertia of the system (in particular, the end effector itself) causing less motion due

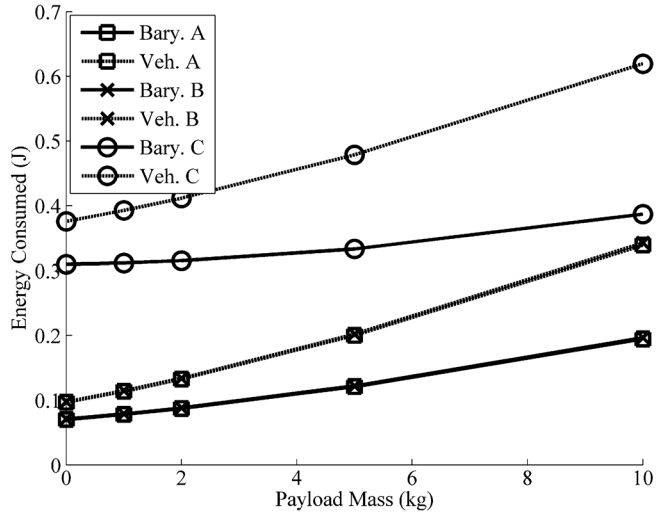

Fig. 15. Energy consumed for various payload masses with (A) stagnant conditions with no density error; (B) stagnant conditions with density error; and (C) unsteady flow conditions with density error.

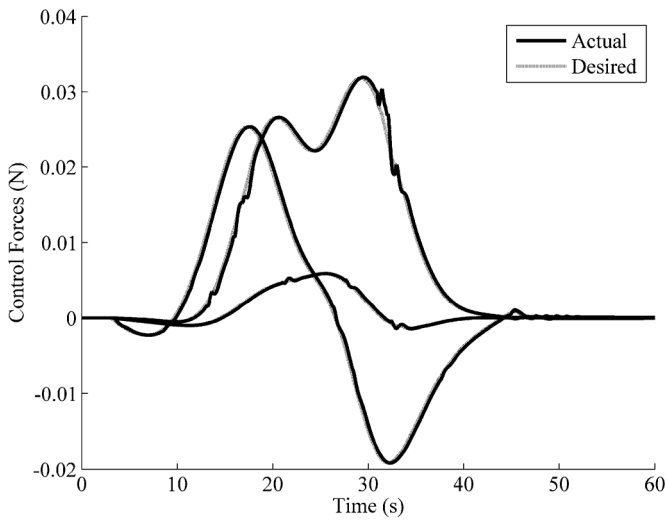

Fig. 16. Comparison of desired and actual control forces for barycenter stabilization under stagnant conditions.

to perturbations. However, Fig. 15 shows that the energy consumed increases geometrically with increasing payload mass. Furthermore, the imposition of unknown unsteady flow of the surrounding fluid causes a significant increase in the consumed energy for both control methods, while the small difference between actual fluid density and that of the model only caused an increase in consumed energy of approximately 1%.

4) Thruster Control: The performance of the thruster control system is evaluated by comparing the desired control forces and moments with those produced by the thrusters. Figs. 16 and Fig. 17 show the desired and actual control forces for barycenter stabilization and vehicle position stabilization under stagnant conditions, respectively. Figs. 18 and 19 show the desired and actual control forces for barycenter stabilization and vehicle position stabilization with unsteady flow and fluid density error, respectively. Although there are small deviations from the desired control input, the overall performance is stable and accurate.

The components of propeller thrust contributing to attitude control and position control are also analyzed. Figs. 20 and

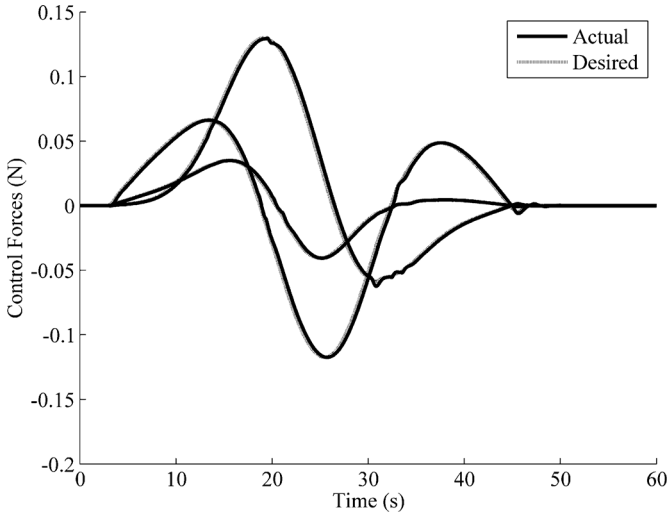

Fig. 17. Comparison of desired and actual control forces for vehicle position stabilization under stagnant conditions.

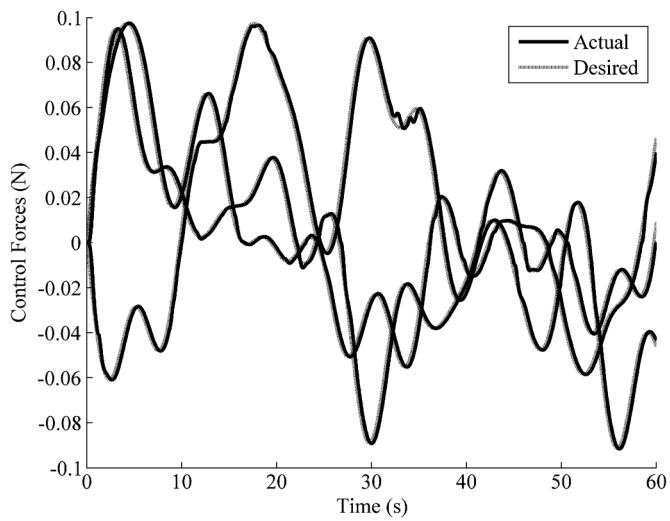

Fig. 18. Comparison of desired and actual control forces for barycenter stabilization with unsteady flow and density error.

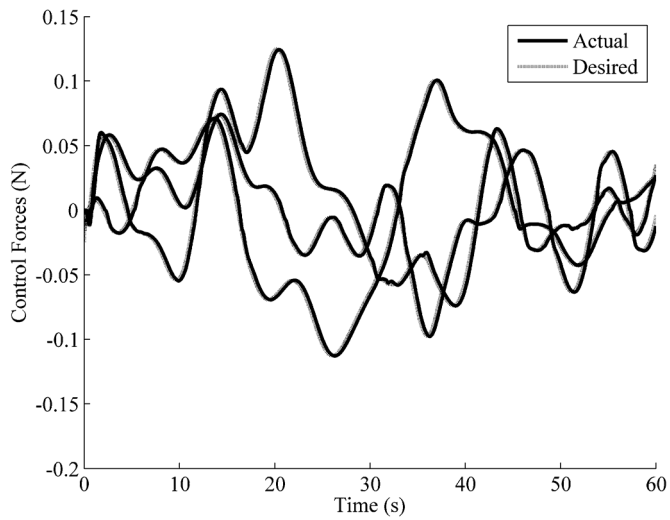

Fig. 19. Comparison of desired and actual control forces for vehicle position stabilization with unsteady flow and density error.

21 show the components of thrust for barycenter stabilization and vehicle position stabilization under stagnant conditions,

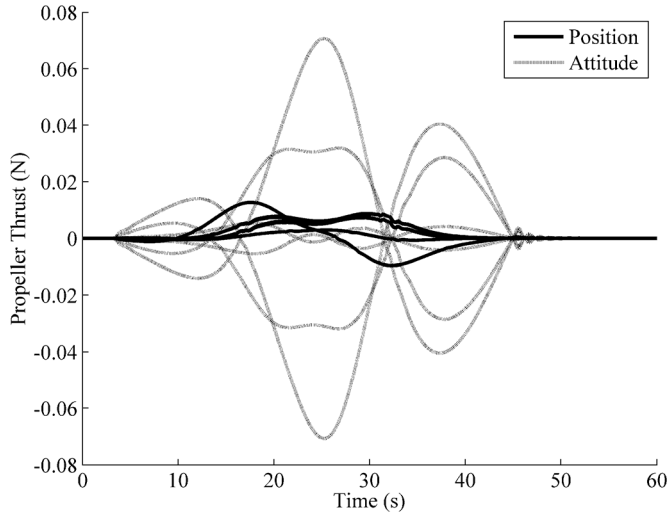

Fig. 20. Comparison of position and attitude components of propeller thrust for barycenter stabilization under stagnant conditions.

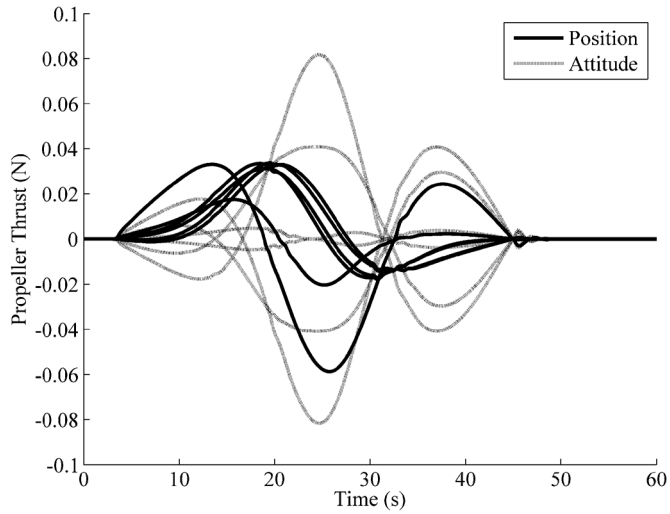

Fig. 21. Comparison of position and attitude components of propeller thrust for vehicle position stabilization under stagnant conditions.

respectively. Figs. 22 and 23 show the components of thrust for barycenter stabilization and vehicle position stabilization with unsteady flow and fluid density error, respectively. The component of propeller thrust for attitude control is similar in both barycenter and vehicle position stabilization cases, and is greater than the component of thrust for position control. However, the component of propeller thrust for position control is much larger in the vehicle position stabilization case than in the barycenter stabilization case. As can be seen in Figs. 22 and 23, the introduction of unsteady flow requires greater propeller thrust as the feedback control terms become much larger, however vehicle stabilization still requires greater thrust for position control than barycenter stabilization.

5) Hydrodynamic Model Fidelity: The level of detail within the hydrodynamic model is of particular importance since this research is currently limited to simulation. A complete computational fluid dynamics model would be preferred to capture the complex flow properties that are expected during motion of the vehicle–manipulator system. However, the implementation of such a model is too complex for the scope of this study. Instead, the simplified hydrodynamic model described previously

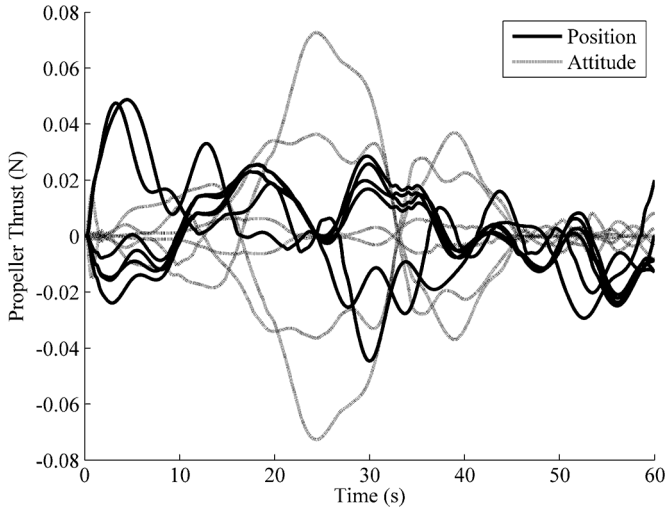

Fig. 22. Comparison of position and attitude components of propeller thrust for barycenter stabilization with unsteady flow and density error.

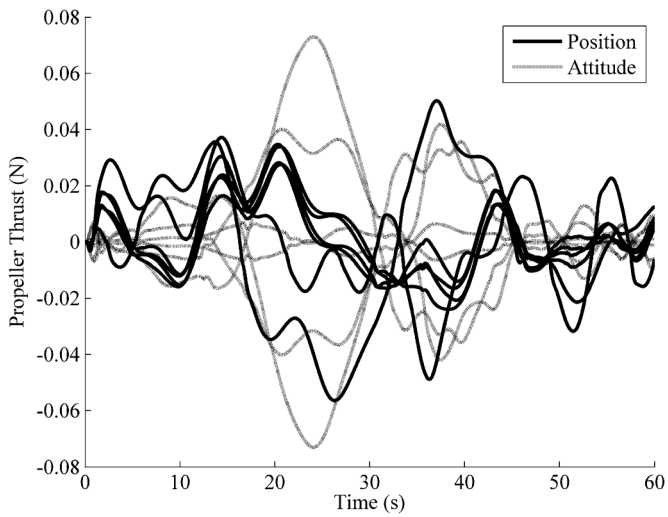

Fig. 23. Comparison of position and attitude components of propeller thrust for vehicle position stabilization with unsteady flow and density error.

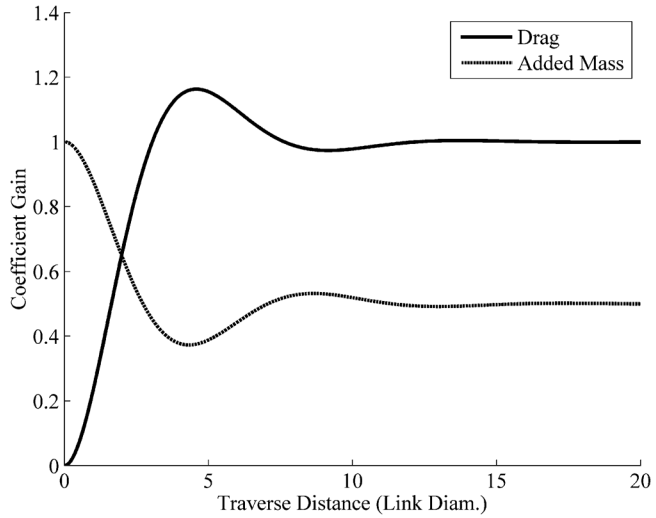

Fig. 24. Variation in drag and added mass coefficients as a function of link traverse distance (expressed in multiples of link diameter).

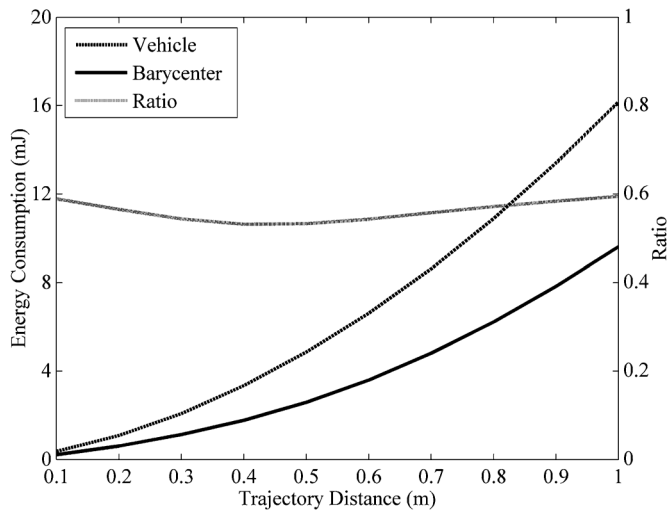

Fig. 25. Comparison of energy consumption for vehicle and barycenter stabilization with varying end-effector travel distance.

is used, including a quadratic drag law, added mass effects, and the impact of angle of attack. Furthermore, deviations between the modeled and actual hydrodynamic forces are imposed using unknown unsteady flow perturbations and differing values of fluid density. Another effect which has not been included is the variation in drag and added mass coefficients due to the transient development of flow characteristics as the manipulator and the vehicle move through their respective trajectories. The variation in these coefficients has been studied by McLain and Rock [36], who demonstrated that the drag and added mass coefficients are functions of the distance traveled by a manipulator link alone. Although this assertion assumes that the link is cylindrical and under constant acceleration, the same variation in the hydrodynamic coefficients is applied within the current model, according to Fig. 24. A comparison of the simulation results with various combinations of each hydrodynamic model detail is shown in Table XIII, where the added mass effects are included in each case. The ratio of energy consumption does not appear to vary greatly depending upon the level of detail within the hydrodynamic model. Therefore, it is expected that the benefits of using barycenter stabilization over vehicle stabilization would be seen during experimental testing and application under real hydrodynamic conditions.

6) Influence of Trajectory Distance: The benefits of barycenter stabilization over vehicle stabilization are also investigated for varying end-effector trajectory travel distances. The end effector is commanded to move purely along the x-axis over a set of travel distances, and the total energy consumed is determined for both barycenter and vehicle stabilization methods. Perturbations from unsteady flow are omitted but error in the modeled fluid density is included as well as the varying drag and added mass coefficients introduced in Section IV-C5. Fig. 25 compares the results of barycenter and vehicle stabilization for end-effector trajectory travel distances between 0.1 and 1 m, as well as the ratio of energy consumed between the two cases. The simulation results show that the ratio of energy consumption is only marginally dependent upon the end-effector travel during the maneuver, remaining within approximately 53%–59%.

7) Influence of Trajectory Duration: The effect of varying the time duration of the end-effector trajectory is also investigated using the same maneuver but over various time dura-

TABLE XIII
END-EFFECTOR ERROR AND ENERGY CONSUMPTION (UNSTEADY CONDITIONS)

Hydrodynamic Model Effects				Energy Consumption (J)		
Unsteady Flow Perturbations	Density Error	Angle-of-Attack	Variable CD & CM	Veh. Stabilization	Barycenter Stabilization	Ratio
x				0.5170	0.3461	0.6695
x	x			0.5223	0.3503	0.6707
x	x	x		0.5030	0.3381	0.6721
x	x	x	x	0.4569	0.2807	0.6144
				0.3331	0.1914	0.5746
	x			0.3365	0.1936	0.5752
	x	x		0.3246	0.1838	0.5661
	x	x	x	0.3187	0.1866	0.5854

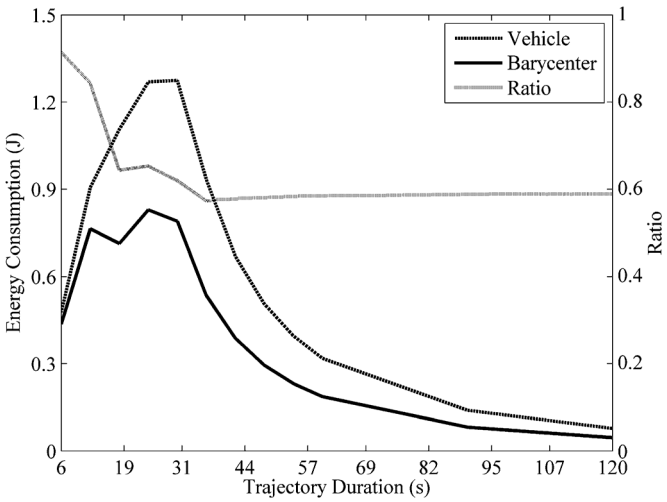

Fig. 26. Comparison of energy consumption for vehicle and barycenter stabilization with varying end-effector trajectory duration time.

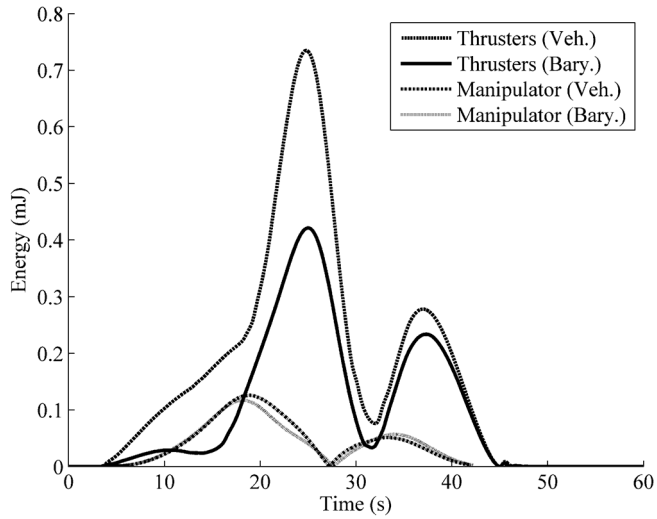

Fig. 27. Comparison of energy consumption of thruster control and manipulator actuation systems for barycenter and vehicle stabilization.

tions. The end effector is commanded to follow the same trajectory as investigated in Section IV-C2, and the total energy consumed is determined for the barycenter and vehicle stabilization methods. Unsteady flow perturbations are ignored while fluid density error is modeled along with varying drag and added mass coefficients. Fig. 26 compares the results of barycenter and vehicle stabilization for end-effector trajectory duration times between 6 and 120 s, as well as the ratio of energy consumed between the two cases. The results of the simulations demonstrate a region of greater dependency upon trajectory duration occurring at low duration times, whereas there is negligible dependency at duration times higher than 30 s. Overall, however, the ratio of energy consumed remains below 100% for all trajectory duration times, suggesting that the barycenter stabilization method is more efficient.

8) Energy Savings Distribution: The reduction in consumed energy is attributed to the decrease in thruster effort required when the vehicle is permitted to translate since the reaction forces due to the motion of the manipulator are not compensated. Therefore, reduction in consumed energy occurs along the entire trajectory since the reaction forces are lower at all times. It is also important to note that the consumed energy is determined for the thruster system only, while the energy consumed for manipulator control is previously not included. Energy consumed by the manipulator is estimated from the torque and speed of each joint, and compared for both barycenter and vehicle stabilization methods. Fig. 27 shows the resulting energy consumption for the thruster system and manipulator actuation system using both stabilization methods. The reduction in energy consumption for the thruster system is significant, while the difference in energy consumption for the manipulator system is negligible.

9) Simplified Analytical Model: Stabilization of the system barycenter requires that energy be consumed for compensation of the hydrodynamic effects alone, while stabilization of the vehicle position requires that energy be consumed for both compensation of the hydrodynamic effects as well as the mechanical work in displacing the system barycenter. However, stabilization of the barycenter requires that hydrodynamic effects upon the vehicle due to its movement be also compensated. Under certain conditions, the hydrodynamic forces on the vehicle during barycenter stabilization may be larger than the reaction forces during vehicle stabilization. For example, if the fluid is extremely dense or viscous, then more energy may be consumed in compensating for vehicle drag than would be consumed in maintaining a fixed vehicle position.

The energy consumed by the controller is proportional to the propeller thrusts, therefore the net control forces acting on the

vehicle body are proportional to the required energy input. The following analysis is used to compare the theoretical control forces for barycenter stabilization and vehicle position stabilization for a simplified vehicle–manipulator model. It is assumed the manipulator links are massless and experience no drag, and that the manipulator end effector is directed in a straight line trajectory following a cosine profile. For barycenter stabilization, the barycenter remains fixed and the position of the vehicle and end effector are related by

$$m_0 x + m_p(x + r) = (m_0 + m_P)x_{cm} \tag{72}$$

where m_0 is the mass of the vehicle, m_P is the mass of the payload, x is the position of the vehicle in inertial coordinates, r is the position of the payload with respect to the vehicle, and x_{cm} is the position of the center of mass

Rearranging (72) yields (73), where η is the ratio of payload mass to the total mass of the system, as defined by

$$x + \eta r = x_{cm} \tag{73}$$

$$\eta = \frac{m_P}{m_0 + m_P}. \tag{74}$$

Differentiation of (73) results in the equations for velocity and acceleration, where it is assumed that the barycenter is stabilized. Therefore, the velocity and acceleration of the vehicle are given, respectively, by

$$\dot{x} = -\eta \dot{r} \tag{75}$$

$$\ddot{x} = -\eta \ddot{r}. \tag{76}$$

From (19), the drag on the vehicle is given by

$$D_0 = \frac{1}{2}\rho C_{D0} A_0 \dot{x}^2. \tag{77}$$

The trajectory of the end effector is defined by

$$r = \frac{r_\Delta}{2}\left(1 - \cos\left(\frac{\pi t}{t_F}\right)\right) + r_0 \tag{78}$$

where the end effector moves a distance r_Δ smoothly from an initial position r_0, over a period of t_F. The velocity and acceleration of the end effector are given, respectively, by

$$\dot{r} = \frac{r_\Delta \pi}{2t_F}\sin\left(\frac{\pi t}{t_F}\right) \tag{79}$$

$$\ddot{r} = \frac{r_\Delta \pi^2}{2t_F^2}\cos\left(\frac{\pi t}{t_F}\right) \tag{80}$$

Therefore, the drag on the vehicle is given by

$$D_0 = \frac{1}{8}\left(\frac{\rho C_{D0} A_0 \eta^2 r_\Delta^2 \pi^2}{t_F^2}\right)\sin^2\left(\frac{\pi t}{t_F}\right). \tag{81}$$

In the case of vehicle position stabilization, the manipulator motion is shortened to reach the same final position in inertial coordinates. The actual end-effector travel x_E is given by

$$\Delta x_E = \Delta x + \Delta r \tag{82}$$

where the vehicle motion is given by

$$\Delta x = -\eta \Delta r \tag{83}$$

which results in

$$\Delta x_E = (1 - \eta)\Delta r. \tag{84}$$

Therefore, to reach the same position in inertial coordinates as the barycenter stabilization case, the end-effector trajectory for the vehicle stabilization case is scaled by a factor of $(1 - \eta)$. The reaction force on the vehicle during vehicle stabilization is given by

$$F_0 = m_P(1 - \eta)\ddot{r} \tag{85}$$

which can be written as

$$F_0 = \frac{1}{2}\left(\frac{m_0 r_\Delta \pi^2 \eta}{t_F^2}\right)\cos\left(\frac{\pi t}{t_F}\right) \tag{86}$$

after substitution of (80) and (74).

The total energy consumed is related to the integral of the control forces over the entire simulation, which are defined as

$$\tilde{D}_0 = \frac{1}{16}\left(\frac{\rho C_{D0} A_0 \eta^2 r_\Delta^2 \pi^2}{t_F}\right) \tag{87}$$

for barycenter stabilization and

$$\tilde{F}_0 = \frac{m_0 r_\Delta \pi \eta}{t_F} \tag{88}$$

for vehicle position stabilization (assuming absolute values of the respective forces). The ratio of integrated drag forces during barycenter stabilization to integrated reaction forces during vehicle position stabilization, defined by

$$\frac{\tilde{D}_0}{\tilde{F}_0} = \frac{\pi}{16}\left(\frac{\rho C_{D0} A_0 r_\Delta}{m_0}\right)\eta \tag{89}$$

is representative of the ratio of energy consumed for the two scenarios.

Now it can be seen that the ratio of vehicle drag during barycenter stabilization to reaction forces during vehicle position stabilization is a function of fluid density ρ and vehicle drag parameters C_{D0} and A_0, as well as the end-effector travel distance r_Δ, vehicle mass m_0, and ratio of payload mass to total system mass η.

If the ratio given by (89) is greater than 1, the drag forces during barycenter stabilization are greater than the reaction forces during vehicle position stabilization, and therefore vehicle stabilization would result in lower energy consumption. Hence, evaluation of (89) allows one to predict which of the two control methods would be more efficient. The maximum possible value of the ratio may be checked by substituting r_Δ with the maximum reach of the manipulator, and equating η to 1. If this maximum value is less than 1, then barycenter stabilization will be more energy efficient for any trajectory and any size payload. However, if the maximum value of (89) is greater than 1, then there exists a maximum payload mass for which barycenter stabilization is preferred for a given end-effector travel distance, as well as a maximum travel distance for a given payload mass.

After substitution of the environment and vehicle parameters used for simulation, the maximum payload mass and maximum end-effector travel distance may be determined. For the absolute maximum end-effector travel distance of the Barrett WAM, $r_\Delta = 1.82$ m, the maximum payload mass is 144.3 kg. Conversely, if the payload mass is unrestricted and $\eta = 1$, the maximum travel distance is 0.994 m. Therefore, if the manipulator motion is restricted to a travel distance equal to or less than 0.994 m, barycenter stabilization will always be more efficient than vehicle position stabilization for any payload mass, whereas if the manipulator motion is unrestricted, then barycenter stabilization is only beneficial up to a payload mass of 144.3 kg. While this payload mass is likely larger than the maximum expected payload for this vehicle–manipulator system, there does exist a configuration in which vehicle position stabilization is more efficient than barycenter stabilization.

V. Conclusion

Effective manipulator position control is demonstrated in simulation through stabilization of the vehicle orientation and system barycenter or vehicle position using combinations of feedback and feedforward control. Stabilization of the system barycenter resulted in lower energy consumption compared to stabilization of the vehicle position under stagnant conditions as well as with the inclusion of unknown unsteady flow and differences between the actual and modeled fluid density. However, it is possible that vehicle position stabilization is more energy efficient if the amount of drag on the vehicle during barycenter stabilization is larger than the required reaction forces for vehicle position stabilization. Therefore, the environmental conditions, vehicle parameters, payload mass, and manipulator travel distance must all be considered to determine which control method is most efficient for a given payload mass and end-effector trajectory. It must also be noted that the suggested barycenter vehicle control algorithm is independent of the manipulator control algorithm and may be applied within other control strategies with more robust manipulator control, end-effector force control, or desired vehicle motion control. The improvement in energy efficiency would prove beneficial for untethered vehicles, especially planetary exploration submersibles such as those proposed for missions to Europa and Enceladus. Although a detailed hydrodynamic model was used in simulation, the complex nature of fluid flow during manipulator motion is difficult to capture. Consequently, supporting experimental verification of the simulation results is required to definitively conclude that the proposed barycenter stabilization method is more energy efficient than vehicle stabilization.

References

[1] J. C. Ellis-Evans, "Sub-glacial Lake Vostok: A possible analogue for a European ocean?," *J. British Interplanetary Soc.*, vol. 54, pp. 159–168, 2001.

[2] M. J. Siegert, A. Behar, M. Bentley, D. Blake, S. Bowden, P. Christoffersen, C. Cockell, H. Corr, D. C. Cullen, H. Edwards, A. Ellery, C. Ellis-Evans, G. Griffiths, R. Hindmarsh, D. A. Hodgson, E. King, H. Lamb, L. Lane, K. Makinson, M. Mowlem, J. Parnell, D. A. Pearce, J. Priscu, A. Rivera, M. A. Sephton, M. R. Sims, A. M. Smith, M. Tranter, J. L. Wadham, G. Wilson, and J. Woodward, "Exploration of Ellsworth subglacial lake: A concept for the development, organization and execution of an experiment to explore, measure and sample the environment of a West Antarctic subglacial lake," *Rev. Environ. Sci. Biotechnol.*, vol. 6, no. 1–3, pp. 161–179, 2007.

[3] R. Pappalardo, M. J. S. Belton, H. H. Breneman, M. H. Carr, C. R. Chapman, G. C. Collins, T. Denk, S. Fagents, P. E. Geissler, B. Giese, R. Greeley, R. Greenberg, J. W. Head, P. Helfenstein, G. Hoppa, S. D. Kadel, K. P. Klaasen, J. E. Klemaszewski, K. Magee, A. S. McEwen, J. M. Moore, W. B. Moore, G. Neukum, C. B. Phillips, L. M. Prockter, G. Schubert, D. A. Senske, R. J. Sullivan, B. R. Tufts, E. P. Turtle, R. Wagner, and K. K. Williams, "Does Europa have a subsurface ocean? Evaluation of the geological evidence," *J. Geophys. Res.*, vol. 104, pp. 24015–24055, 1999.

[4] J. Powell, G. Maise, and J. Paniagua, "NEMO: A mission to search for and return to Earth possible life forms on Europa," *Acta Astronautica*, vol. 57, pp. 579–593, 2005.

[5] S. Di Pippo, R. Mugnuolo, P. Vielmo, and W. Prendin, "Exploitation of Europa ice and water basins: An assessment on required technological developments, on system design approaches and on relevant expected benefits to space and Earth based activities," *Planetary Space Sci.*, vol. 47, pp. 921–933, 1999.

[6] F. Carsey, G. S. Chen, J. Cutts, L. French, R. Kern, A. Lane, P. Stolorz, and W. Zimmerman, "Exploring Europa's ocean: A challenge for marine technology of this century," *J. Mar. Technol. Soc.*, vol. 33, pp. 5–12, 2000.

[7] H. Jannasch, "Chemosynthetic support of life and the microbial diversity at deep sea hydrothermal vents," *Proc. Roy. Soc. Lond.*, vol. B225, pp. 277–297, 1985.

[8] D. Rothery, "Europa and other icy satellites as possible abodes of life," *J. British Interplanetary Soc.*, vol. 54, pp. 153–158, 2001.

[9] J. Corliss, J. Baross, and S. Hoffman, "Hypothesis concerning the relationship between submarine hot springs and the origin of life on Earth," *Oceanologica Acta*, vol. 4, pp. 59–69, 1981.

[10] J. Baross and S. Hoffman, "Submarine hydrothermal vents and associated gradient environments as sites for the origin and evolution of life," *Origins of Life*, vol. 15, pp. 327–345, 1985.

[11] M. Russell and A. Hall, "Emergence of life from iron monosulphide bubbles at a submarine hydrothermal redox and pH front," *J. Geological Soc.*, vol. 154, pp. 377–402, 1997.

[12] N. Holm and E. Anderson, "Abiotic synthesis of organic compounds under the conditions of submarine hydrothermal systems: A perspective," *Planetary Space Sci.*, vol. 43, no. 1/2, pp. 153–159, 1995.

[13] M. Di Giulo, "Universal ancestor was a thermophile or a hyperthermophile: Tests and further evidence," *J. Theor. Biol.*, vol. 221, pp. 425–436, 2003.

[14] R. Huber, H. Huber, and K. Stetter, "Towards the ecology of hyperthermophiles: Biotopes, new isolation strategies and novel metabolic properties," *FEMS Microbiol. Rev.*, vol. 24, pp. 615–623, 2000.

[15] N. Leonard, "Control synthesis and adaptation of an underactuated autonomous underwater vehicle," *IEEE J. Ocean. Eng.*, vol. 20, no. 3, pp. 211–220, Jul. 1995.

[16] C. R. Carignan and D. L. Akin, "The reaction stabilization of on-orbit robots," *IEEE Control Syst. Mag.*, vol. 20, no. 6, pp. 19–33, Dec. 2000.

[17] F. Bruhn, F. Carsey, J. Kohler, M. Mowlem, C. German, and A. Behar, "MEMS enablement and analysis of the miniature autonomous submersible explorer," *IEEE J. Ocean. Eng.*, vol. 30, no. 1, pp. 165–178, Jan. 2005.

[18] D. Yoerger and J. Slotine, "Robust trajectory control of underwater vehicles," *IEEE J. Ocean. Eng.*, vol. OE-10, no. 4, pp. 462–470, Oct. 1985.

[19] R. Cox and S. Wei, "Advances in the state of the art for AUV inertial sensors and navigation systems," *IEEE J. Ocean. Eng.*, vol. 20, no. 4, pp. 361–366, Oct. 1995.

[20] G. Antonelli, F. Caccavale, S. Chiaverini, and L. Villani, "Tracking control for underwater vehicle-manipulator systems with velocity estimation," *IEEE J. Ocean. Eng.*, vol. 25, no. 3, pp. 399–413, Jul. 2000.

[21] L. Hsu, R. Costa, F. Lizarralde, and J. da Cunha, "Dynamic positioning of remotely operated underwater vehicles," *IEEE Robot. Autom. Mag.*, vol. 7, no. 3, pp. 21–31, Sep. 2000.

[22] P. Webb, "Maneuverability: General issues," *IEEE J. Ocean. Eng.*, vol. 29, no. 3, pp. 547–555, Jul. 2004.

[23] A. Ellery, "An engineering approach to the dynamic control of space robotic on-orbit servicers," *Proc. Inst. Mech. Eng. G, Aerosp. Eng.*, vol. 218, pp. 79–98, 2004.
[24] A. Ellery, "Robotic in-orbit servicers—The need for control moment gyroscopes for attitude control," *Aeronaut. J. Roy. Aeronaut. Soc.*, vol. 108, no. 1082, pp. 207–214, 2004.
[25] L. Lapierre, P. Fraisse, and N. K. M'Sirdi, "Hybrid position/force control of a ROV with a manipulator," in *Proc. OCEANS Conf.*, Sep. 1998, vol. 2, pp. 931–935.
[26] P. Fraisse, L. Lapierre, P. Dauchez, and F. Pierrot, "Position/force control of an underwater vehicle equipped with a robotic manipulator," in *Proc. 6th IFAC Symp.*, 2001, vol. 2, pp. 513–517.
[27] R. W. Longman, R. E. Lindberg, and M. F. Zedd, "Satellite-mounted robot manipulators—New kinematics and reaction moment compensation," *Int. J. Robot. Res.*, vol. 6, no. 3, pp. 87–103, 1987.
[28] T. Fossen and M. Blanke, "Nonlinear output feedback control of underwater vehicle propellers using feedback form estimated axial flow velocity," *IEEE J. Ocean. Eng.*, vol. 25, no. 2, pp. 241–255, Apr. 2000.
[29] Y. Kim and H. Choi, "An adaptive and robust controller for the undersea robot manipulator," *Int. J. Korean Soc. Precision Eng.*, vol. 4, no. 2, pp. 13–22, 2003.
[30] Barrett Technology Inc., "WAM Arm Datasheet," 2011 [Online]. Available: http://www.barrett.com/robot/DS_WAM.pdf
[31] J. Yuh, "A neural net controller for underwater robotic vehicles," *IEEE J. Ocean. Eng.*, vol. 15, no. 3, pp. 161–166, Jul. 1990.
[32] J. Yuh and R. Lakshmi, "Control of underwater robots in working mode," in *Proc. IEEE Int. Conf. Robot. Autom.*, 1991, pp. 2630–2635.
[33] S. McMillan, D. Orin, and R. McGhee, "A computational framework for simulation of underwater robotic vehicle systems," *Autonom. Robots*, vol. 3, pp. 253–268, 1996.
[34] T. Tarn, G. Shoults, and S. Yang, "A dynamic model of an underwater vehicle with a robotic manipulator using Kane's method," *Autonom. Robots*, vol. 3, pp. 269–283, 1996.
[35] T. McLain, S. Rock, and M. Lee, "Experiments in the coordinated control of an underwater arm/vehicle system," *Autonom. Robots*, vol. 3, pp. 213–232, 1996.
[36] T. McLain and S. Rock, "Development and experimental validation of an underwater manipulator hydrodynamic model," *Int. J. Robot. Res.*, vol. 17, no. 7, pp. 748–759, 1998.
[37] K. Leabourne and S. Rock, "Model development of an underwater manipulator for coordinated arm-vehicle control," in *Proc. IEEE OCEANS Conf.*, 1998, pp. 941–946.
[38] S. Dubowsky and E. Papadopoulos, "The kinematics, dynamics, and control of free-flying and free-floating space robotic systems," *IEEE Trans. Robot. Autom.*, vol. 9, no. 5, pp. 531–543, Oct. 1993.
[39] E. Koval, "Automatic stabilization system of underwater manipulation robot," in *Proc. IEEE OCEANS Conf.*, 1994, pp. 807–812.
[40] K. Leabourne, S. Rock, S. Fleischer, and R. Burton, "Station keeping of an ROV using vision technology," in *Proc. MTS/IEEE OCEANS Conf.*, , vol. 1, pp. 634–640.
[41] G. Antonelli and S. Chiaverini, "Adaptive tracking control of underwater vehicle-manipulator systems," in *Proc. IEEE Conf. Control Appl.*, 1998, pp. 1089–1093.
[42] D. Yoerger, H. Schempf, and D. DiPietro, "Design and performance evaluation of an actively compliant underwater manipulator for full-ocean depth," *J. Robot. Syst.*, vol. 8, no. 3, pp. 371–392, 1991.
[43] G. Antonelli, F. Caccavale, S. Chiaverini, and L. Villani, "Tracking control for underwater vehicle-manipulator systems with velocity estimation," *IEEE J. Ocean. Eng.*, vol. 25, no. 3, pp. 399–413, Jul. 2000.
[44] G. Antonelli, N. Sarkar, and S. Chiaverini, "Explicit force control for underwater vehicle-manipulator systems," *Robotica*, vol. 20, pp. 251–260, 2002.
[45] G. Antonelli and S. Chiaverini, "Fuzzy redundancy resolution and motion coordination for underwater vehicle-manipulator systems," *IEEE Trans. Fuzzy Syst.*, vol. 11, no. 1, pp. 109–120, Feb. 2003.
[46] G. Antonelli, F. Caccavale, and S. Chiaverini, "Adaptive tracking control of underwater vehicle-manipulator systems based on the virtual decomposition approach," *IEEE Trans. Robot. Autom.*, vol. 20, no. 3, pp. 594–602, Jun. 2004.
[47] P. Sanz, P. Ridao, G. Oliver, C. Melchiorri, G. Casalino, C. Silvestre, Y. Petillot, and A. Turetta, "TRIDENT: A framework for autonomous underwater intervention missions with dexterous manipulation capabilities," in *Proc. 7th IFAC Symp. Intell. Autonom. Veh.*, 2010, vol. 7, no. 1, pp. 187–192.

Brian Lynch received the Bachelor of Engineering, Master of Applied Sciences, and Doctor of Philosophy degrees from the Department of Mechanical & Aerospace Engineering, Carleton University, Ottawa, ON, Canada, in 2006, 2007, and 2013, respectively. All three degrees were in the field of aerospace engineering, with his undergraduate degree having a focus on structures, systems, and vehicle design. He completed his M.S. degree while part of the Carleton University Rotorcraft Research Group, where he participated in the development of a smart rotor blade for reducing noise and vibration in helicopters. His thesis, titled "Investigation of shape memory alloy wire for closed loop angular position control of a shaft under random excitation," examined the use of shape memory alloy wires as actuators for an articulated rotor blade tip.

Upon graduation, he joined the Canadian Space Agency as a Research Affiliate to complete his doctoral research. This research concentrates on the development of a predictive engineering model of the relationships between electrical resistance, applied stress, and strain in shape memory alloy. As part of the Space Exploration Engineering Group at Carleton University, he has also participated in the development of planetary rovers and their subsystems. His passion for research and teaching has led him to pursue an academic career with a focus on space exploration.

Alex Ellery received the B.S. degree in physics (with honors) from the University of Ulster, Londonderry, U.K., in 1988, the M.S. degree in astronomy from the University of Sussex, Brighton, East Sussex, U.K., in 1991, and the Doctor of Philosophy degree in astronautics & space engineering from the Cranfield Institute of Technology, Cranfield, Bedford, U.K., in 1995.

Originally from the Surrey Space Centre in the United Kingdom, he worked on several ESA projects including the ExoMars Rover & Pasteur Payload Phase A study, ExoMars Panoramic Camera, and the ACTs Bionics & Space Systems. He also worked with the U.K. PPARC in investigating the use of optic flow-based reactive navigation for the ExoMars rover. In addition, he developed a Mars microrover mission concept "Vanguard" for astrobiological investigation which was based on the deployment of infrared Raman spectroscopy. He is the holder of a Canada Research Chair in Space Robotics & Space Technology at Carleton University, Ottawa, ON, Canada. He built and currently leads the Space Exploration Engineering Group (SEEG) at Carleton University which concentrates on the area of space robotics/planetary rovers. Since coming to Canada, most of his work has been in support of Canadian Space Agency (CSA) projects. He is the author of the textbook *An Introduction to Space Robotics* (2000). He has two further textbooks forthcoming: *Space Technology for Astrobiology Missions* and *Planetary Rovers: Tools for Space Exploration* (with two coauthors). A fourth textbook, *Space Payloads: Instruments for Astrobiology*, is underway.

Dr. Ellery is a Past President of the Astrobiology Society of Britain and is currently a member of the Canadian Astrobiology Programme. He was one of the founders of the U.K. Penetrator Consortium.